Politecnico di Torino

Politecnico di Torino

Master's Degree in Biomedical Engineering

Academic Year 2025/2026

Development and Evaluation of a Robust ECG-Based Signal Processing Pipeline for Wearable Cardiorespiratory Monitoring

Supervisors:

Prof. Luca Mesin

Prof. Elisabetta Peri

Dr. Alessandra Galli

Candidate:

Gioele Casalino

To my family, who gave me this great opportunity and whose warmth and love have always been present. To my friends—first and foremost as friends rather than colleagues—and to my roommates, with whom I have shared this wonderful journey.

Abstract

Recent studies have shown that cardiovascular diseases remain the leading cause of death worldwide. Since many cardiovascular conditions are characterized by event-related symptoms, the development of wearable devices for long-term electrocardiographic (ECG) monitoring has increased. However, their widespread use requires robust signal processing techniques capable of operating under dynamic conditions.

In real-life scenarios, body movements introduce motion artifacts and muscle interference that degrade ECG signal quality, affecting R-peak detection, heart rate variability (HRV) metrics, and respiratory rate (RR) estimation. This work proposes a robust signal processing pipeline for extracting cardiovascular and respiratory parameters from wearable ECG recordings. The framework includes ECG denoising based on bandpass filtering combined with singular value decomposition (SVD), followed by R-peak detection and subsequent extraction of relevant time-domain HRV metrics. After comparing different R-peak detection strategies, a continuous wavelet transform (CWT)-based algorithm was selected for its superior robustness in wearable applications. Respiratory rate was estimated both directly through embedded bioimpedance sensors and indirectly using ECG-derived respiration (EDR), enabling additional comparison between direct and indirect respiratory features.
The pipeline development phase involved three healthy subjects. The total recording duration was 1473 minutes (24 h 33 min), of which 90.4% was retained for framework development (1331 minutes, i.e., 22 h 11 min) after signal quality assessment.

Moreover, the impact of electrode placement was evaluated by positioning two adhesive dry patches at distinct trunk locations (thoracic and left side) on a healthy subject. Recordings were performed during motion-based task challenges—walking, stair climbing, and jumping—to evaluate the robustness of the developed processing algorithms in the presence of motion-induced artifacts.

Results show that the proposed processing framework enhances ECG delineation, leading to improved R-peak detection reliability and greater stability of HRV and RR estimation under dynamic conditions. Finally, the comparative analysis of electrode placement indicates that thoracic positioning is more reliable under non-stationary conditions, providing researchers with practical guidance for future continuous cardiorespiratory monitoring systems.

Contents

List of Figures

List of Tables

Chapter 1

Introduction

1.1 Context and Motivations

Cardiovascular diseases (CVDs) remain the leading cause of death worldwide [2], highlighting the importance of reliable tools for monitoring cardiac activity. Electrocardiography (ECG) represents one of the most widely used non-invasive techniques for assessing the electrical activity of the heart and provides valuable information about heart rhythm, cardiac conduction, and autonomic regulation. However, many cardiovascular conditions manifest suddenly and are characterized by event-related symptoms, such as arrhythmias, which may not be detected during short clinical examinations. For this reason, continuous ECG monitoring is often required [3].

In recent years, the increasing availability of wearable technologies has enabled long-term physiological monitoring in real-life and ambulatory environments. Wearable devices such as smartwatches [4], wristbands [5], and smart clothing [6] allow unobtrusive and comfortable monitoring during daily activities, outside the traditional clinical setting. Beyond cardiovascular observation, these technologies may also provide information in subjects experiencing sporadic or transient events, such as stress-related episodes, epilepsy, or other neurological conditions [7, 8].

Despite their advantages in terms of cost, portability, and comfort, wearable ECG systems are significantly more susceptible to signal degradation than clinical equipment. Body movements, muscle contractions, and variations in electrode–skin contact introduce motion artifacts, electromyographic (EMG) interference [9], and baseline drift, which can distort the ECG waveform and complicate signal interpretation. These disturbances may also affect the detection of morphological features—such as the QRS complex—and can compromise the reliability of subsequent physiological analyses [10].

In the context of wearable monitoring and stress-related conditions, the extraction of heart rate variability (HRV) metrics is particularly relevant for evaluating autonomic nervous system (ANS) modulation [11]. Fluctuations in heart rate (HR) and beat-to-beat intervals reflect the dynamic balance between sympathetic and parasympathetic activity, which influences cardiovascular and respiratory systems. Consequently, accurate R-peak detection is crucial for reliable HRV estimation and for minimizing misinterpretation of arrhythmic events. Over the past decades, several R-peak detection approaches have been developed, including threshold-based techniques (e.g., the Pan–Tompkins algorithm) and more advanced wavelet transform-based methods.

In addition to cardiac monitoring, wearable technologies increasingly enable the assessment of cardiorespiratory dynamics, providing complementary information on physiological regula-

tion. Respiratory activity is closely linked to cardiac function through mechanisms such as respiratory sinus arrhythmia (RSA) and contributes to autonomic nervous system modulation [12]. For this reason, respiratory rate (RR) estimation has become an important component of wearable monitoring systems. RR can be estimated both directly, through bioimpedance sensors measuring thoracic impedance changes during breathing, and indirectly, through ECG-derived respiration (EDR) techniques based on respiratory-related variations in the ECG signal [13].
In conclusion, addressing these challenges requires the development of a robust signal processing pipelinecapable of enhancing ECG signal quality, accurately detecting cardiac events, and enabling reliable extraction of cardiorespiratory parameters from noisy wearable recordings.

1.2 Research Questions

Based on the challenges outlined in the previous section, this work focuses on three main research questions related to the reliability of wearable cardiorespiratory monitoring systems.

1. **Robustness of Signal Processing Pipeline**: To what extent is the proposed signal processing pipeline able to correctly detect R-peaks in ECG signals acquired with wearable devices during daily activities? Furthermore, how reliable are the HRV metrics subsequently extracted?

2. **Impact of Electrode Placement on ECG Signal Quality**: Does the placement of wearable ECG patches influence signal quality and R-peak detection performance? In particular, is there a patch configuration—between the central thoracic and the left-side trunk locations—that provides more reliable recordings under both resting and dynamic conditions?

3. **Respiratory Rate Estimation in Wearable Systems**: How consistent are the RR values estimated indirectly through EDR signal compared to those obtained directly from the bioimpedance signal?

1.3 Contributions

The main contributions of this work address the research questions outlined above and can be summarized as follows.

1. **Development and Evaluation of a Robust Signal Processing Pipeline**: A signal processing framework is implemented to enhance ECG signal quality, enabling reliable estimation of HRV metrics in wearable recordings affected by motion artifacts. The pipeline includes ECG denoising, R-peak detection using a CWT-based method, computation of beat-to-beat intervals, and subsequent extraction of time-domain variability parameters. The development phase focused on long-term recordings and included the comparison of three different R-peak detection approaches, while the evaluation phase assessed the performance of the developed pipeline during specific daily activities and motion-based tasks.

2. **Experimental Comparison of Electrode Placement**: The impact of electrode placement on ECG signal quality is investigated by comparing two wearable patch configurations placed at different trunk locations (central thoracic and left-side). The analysis

evaluates the reliability of each configuration in terms of signal quality and R-peak detection performance during both resting and dynamic conditions. This comparison aims to provide researchers with practical guidance for future continuous cardiorespiratory monitoring systems.

3. **Comparative Assessment of Respiratory Rate Estimation Methods**: RR is estimated through two complementary approaches: direct measurement using the bioimpedance signal and indirect estimation based on EDR signal. The agreement between these methods is evaluated to assess the feasibility of ECG-based respiratory monitoring in wearable systems.

1.4 Thesis Outline

The remainder of this thesis is organized as follows.

Chapter 2 reviews the current state of the art. It first presents the physiological background related to stress and autonomic nervous system activity, together with the main cardiac and respiratory features considered in this work, namely heart rate (HR), heart rate variability (HRV), and respiratory rate (RR). The chapter then discusses wearable physiological monitoring systems, their opportunities and limitations, and finally reviews the main signal processing approaches for wearable ECG analysis, with particular focus on filtering techniques and QRS detection methods.

Chapter 3 describes the materials and methods adopted in this study. It presents the experimental design, the wearable device and acquisition setup, and the datasets used for both the development and evaluation phases. The chapter then details the proposed signal processing pipeline, and the criteria used for signal quality assessment and algorithm evaluation.

Chapter 4 presents and discusses the results obtained during both the development and evaluation phases. The chapter first reports the results related to signal quality assessment and the comparison between R-peak detection methods. It then analyzes the evaluation phase results, including the comparison of electrode patch placements, the analysis of HR and HRV metrics across activities, and the comparison of RR estimation methods.

Finally, Chapter 5 summarizes the main findings of this work, discusses the main limitations of the study, and outlines possible directions for future research.

Chapter 2

State of the Art

2.1 Physiological Background

2.1.1 Stress and Autonomic Nervous System (ANS)

The anatomic distribution of autonomic nervous system (ANS) is extended to several organ systems within the human body. The ANS governs a wide range of essential involuntary physiological functions, including blood pressure, heart rate, respiration, gastrointestinal activity, pupillary responses, and sexual function. The ANS consists of two major branches: the sympathetic nervous system (SNS), and parasympathetic nervous system (PNS), which synergize to control multiple opposing and complementary body's functions [14].
The SNS promotes energy mobilization and prepares the body for action in response to perceived threats, in what is commonly described as the *"fight-or-flight"* response. Conversely, the PNS—whose main efferent pathway is the vagus nerve—is responsible for the *"rest-and-digest"* response, facilitating recovery, restoration, and conservation of energy. Importantly, SNS and PNS activities are not strictly antagonistic: many physiological responses arise from coordinated co-activation of both systems.
The ANS plays a crucial role in the experience of emotions and responses to environmental stressors [7]. Vagal efferent activity is associated with social engagement, regulation of emotional states, and perception of safety. The vagus also mediates the stress response in other organs such as the bronchi, esophagus, pharynx and heart. Stress and anxiety inhibit vagal tone and shift autonomic balance toward sympathetic dominance—which is considered crucial to appropriately react to external threats—leading to characteristic cardiorespiratory changes such as increased heart rate, reduced heart rate variability, and altered respiratory patterns [14].

2.1.2 ECG signal

The electrocardiogram (ECG) is a non-invasive biosignal that reflects the electrical activity of the heart as a function of time. It represents the electrical changes generated by cardiac muscle depolarization and repolarization through cardiac cycles, and provides indirect information about cardiac rhythm, conduction pathways, and myocardial integrity. Sample ECG signals associated with a common cardiac cycle are illustrated in Fig. 2.1.
ECG recordings are widely used in both clinical practice and research due to their simplicity, low cost, and high diagnostic value, especially for monitoring cardiovascular diseases (CVDs), which is the first cause of death worldwide [15]. Abnormal ECG patterns occur in several

CVDs, including atrial fibrillation [16], ventricular tachycardia [17], myocardial ischemia [18], and myocardial infarction [19].

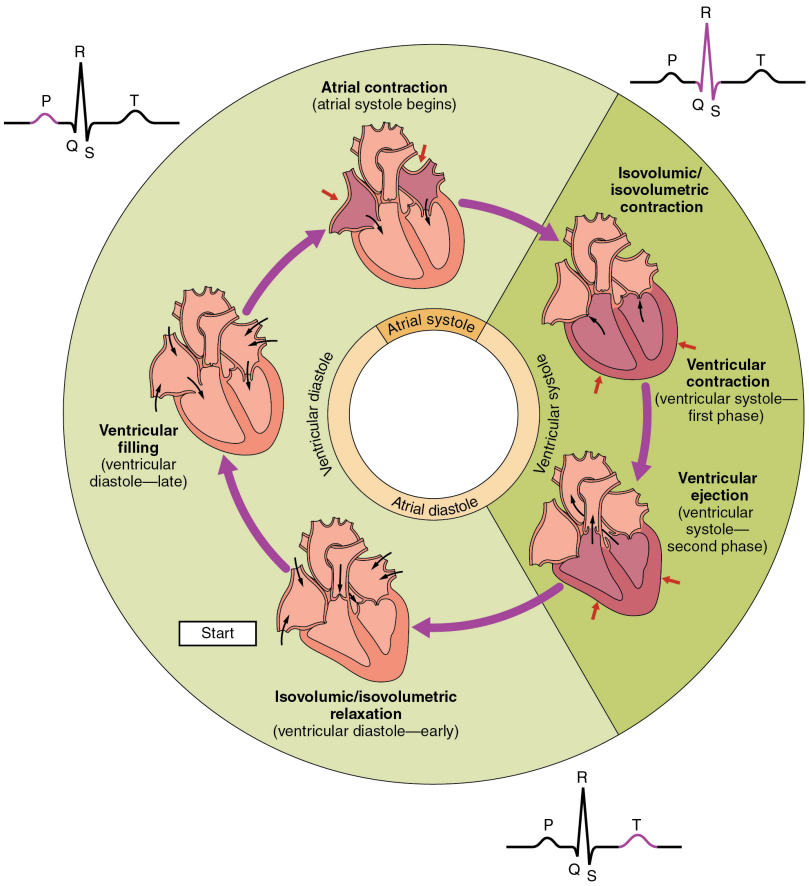

Figure 2.1: Common cardiac cycle with the associated waves of an ECG signal (one-lead recording).

The ECG signal is recorded by measuring potential differences between electrodes placed on the surface of the skin. Standard clinical ECG acquisition uses multiple leads—conventionally 12-lead ECG—to observe cardiac activity from different spatial orientations, however wearable [4, 5] and ambulatory devices [20] often rely on one or few leads to enable continuous long-term monitoring.

A single cardiac cycle in the ECG waveform (Fig. 2.2) is conventionally described by a sequence of characteristic deflections known as fiducial points [21]. These include the QRS complex and P and T waves. The P wave corresponds to atrial depolarization and typically has a duration of less than 120 ms with relatively low amplitude. The QRS complex reflects rapid ventricular depolarization and is the most prominent feature of the ECG, characterized by high amplitude and steep slopes; its normal duration ranges approximately between 70 and 110 ms. The T wave represents ventricular repolarization and generally exhibits a longer duration—typically between 100 and 250 ms—with lower frequency content compared to the QRS complex [3]. In general, ECG morphology varies with heart rate, autonomic modulation, body posture, and physiological or pathological conditions. The main ECG waveform components and their features are described briefly in Table 2.1.
In addition to these morphological components, several clinically relevant temporal intervals can be derived from the ECG, including the PR interval, QT interval, and RR interval. Of

particular importance for heart rate and heart rate variability analysis is the RR interval, defined as the time elapsed between two consecutive R peaks. Accurate identification of these fiducial points—especially the R peak—is therefore a fundamental prerequisite for quantitative ECG analysis and subsequent extraction of autonomic biomarkers [11].

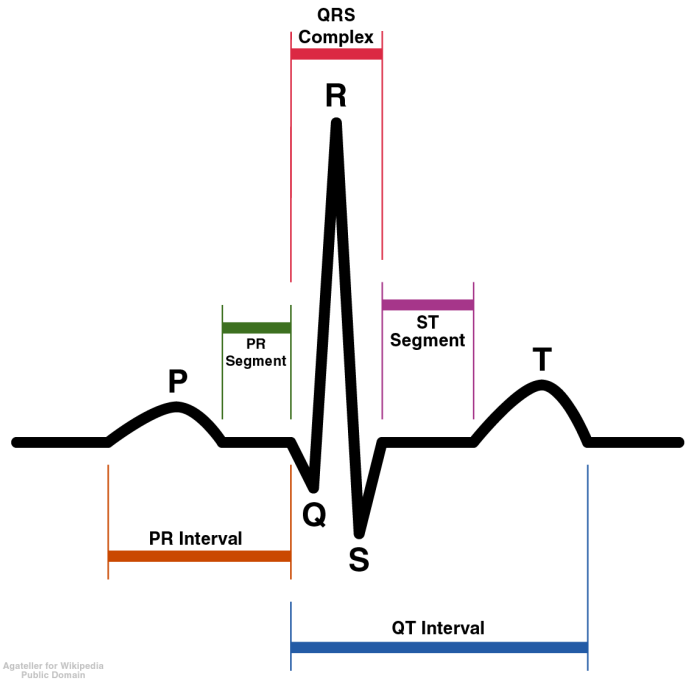

Figure 2.2: Standard fiducial points and relevant segments in the ECG signal.

Table 2.1: Main ECG waveform components and their characteristic.

Waveform	**Event**	**Duration**	**Frequency**
P wave	Atrial depolarization	< 120 ms	Low frequency (< 10 Hz)
QRS complex	Rapid ventricular depolarization	~ 70–110 ms	Broadband, mainly 10–40 Hz
T wave	Ventricular repolarization	~ 100–250 ms	Very low frequency (< 7 Hz)

Overall, the ECG provides valuable information about the electrical activity of the heart, where both the shape of the waveform and the timing between beats reflect physiological and pathological conditions. For this reason, ECG analysis is fundamental for tasks such as beat detection, rhythm evaluation, and assessment of autonomic regulation, especially in long-term and wearable monitoring applications.

2.1.3 Heart Rate (HR)

Heart rate (HR) represents the number of cardiac cycles per unit time, typically expressed in beats per minute (bpm). In healthy adults at rest, HR generally ranges from 60 to 100 bpm [22], whereas trained athletes may show resting values as low as 40–60 bpm due to enhanced

vagal tone and cardiac efficiency [23]. HR is derived from the electrical activity of the heart recorded via ECG, where the interval between two consecutive R-wave peaks corresponds to the duration of one cardiac cycle. HR is therefore inversely related to the RR interval. Accordingly with RR intervals, HR dynamically varies with metabolic demands, physical activity, posture, thermoregulation, and respiratory patterns.
HR changes also shape the temporal window available for beat-to-beat fluctuations: higher HR mechanically restricts variability, whereas lower HR allows greater fluctuation. This intrinsic relationship means that HR exerts both a physiological and mathematical influence on heart rate variability (HRV), which quantifies variations in successive RR intervals.

2.1.4 Heart Rate Variability (HRV)

Heart rate variability (HRV) refers to the physiological fluctuations in the duration of successive RR intervals, reflecting the dynamic interplay between sympathetic and parasympathetic influences on the sinoatrial (SA) node [11, 24]. Sympathetic activation shortens the RR interval by accelerating diastolic depolarization, while parasympathetic activation lengthens it through inhibitory effects on pacemaker cells. As a result, the RR interval naturally oscillates due to variations in autonomic outflow, baroreflex modulation, thermoregulation, and respiratory-driven influences.
Consequently, HRV can be viewed as a stochastic time series in which beats are plotted on the x-axis and the corresponding RR interval duration on the y-axis. The instantaneous HR series can also be derived by converting each RR interval into its equivalent HR value. Importantly, since the variability in HR occurs on a beat-to-beat basis, the RR series is inherently non-uniformly spaced along the x-axis, as shown in Fig. 2.3. This fact leads to complications in metrics that require resampling and interpolation, such as spectral domain parameters [25].

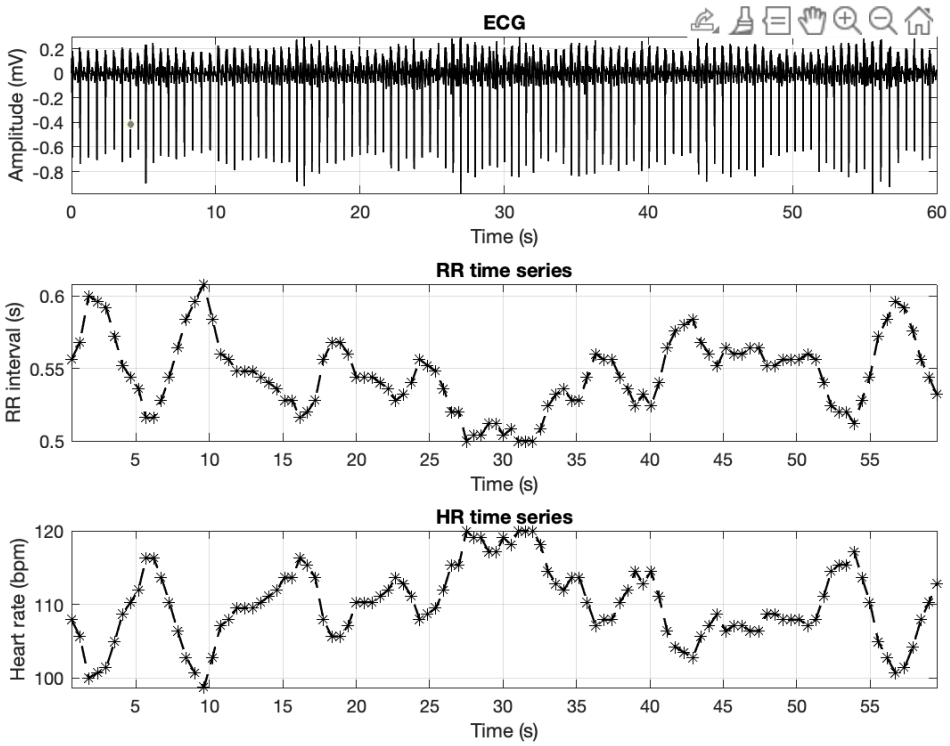

Figure 2.3: Instantaneous and beat-to-beat (star markers) RR interval (middle trace) and corresponding HR (lower trace) for 1 minute segment of ECG (upper trace).

HRV is typically quantified using time-domain and frequency-domain metrics, each capturing different aspects of autonomic regulation. Time-domain measures describe the amount of variability in RR intervals over time, whereas frequency-domain analysis decomposes RR interval oscillations into components associated with specific physiological rhythms [11, 25]. Overall, higher HRV reflects greater autonomic flexibility and the ability to adapt to internal and external demands, whereas reduced HRV is associated with reduced regulatory capacity.

2.1.4.1 Time-domain metrics

Time-domain HRV metrics are computed from the sequence of normal-to-normal (NN) intervals and provide a direct quantification of beat-to-beat variability. Among the most widely used measures are the standard deviation of NN intervals (SDNN), which reflects overall HRV and incorporates both short and long-term components, and the root mean square of successive differences (RMSSD), which is particularly sensitive to short-term variations mediated by parasympathetic activity [11]. Additional time-domain indices include the percentage of successive NN intervals differing by more than 50 ms (pNN50).
Nonlinear time-domain analysis is commonly performed using the Lorenz plot (Fig. 2.4), also known as the Poincaré plot, in which each NN interval is plotted as a function of the following one [1]. This graphical representation provides information on the dynamics of HR regulation beyond simple variance measures. Quantitative descriptors derived from the Lorenz plot include SD1 and SD2, which measure the width and length of the Poincaré cloud, respectively. SD1 reflects short-term, beat-to-beat variability predominantly associated with parasympathetic activity, whereas SD2 captures longer-term variability influenced by both sympathetic and parasympathetic modulation [8, 26].

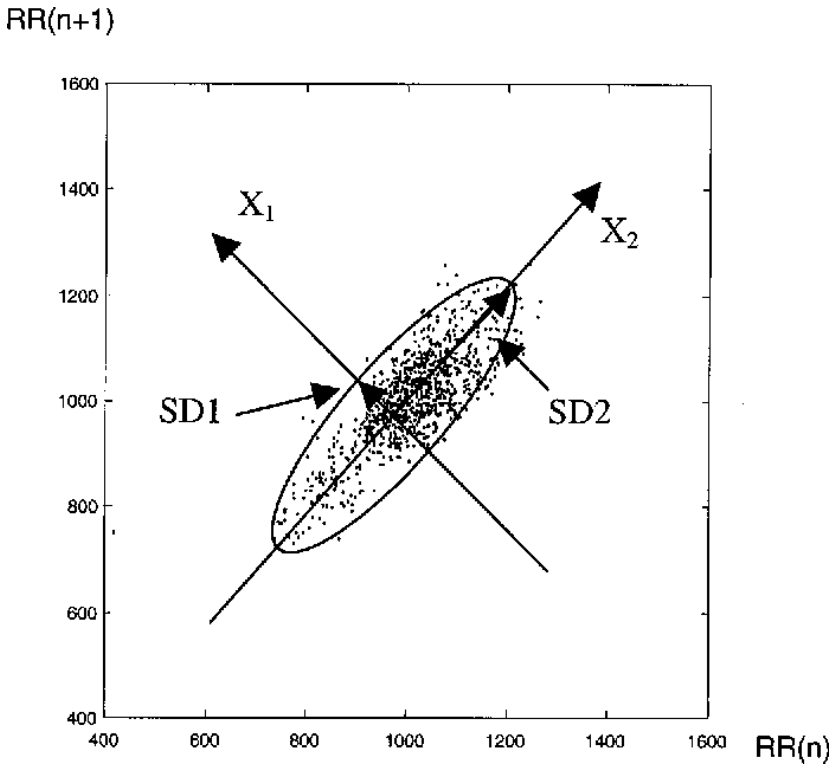

Figure 2.4: An example Poincaré plot from Brennan et Al. [1], depicting a cloud-shaped distribution of points.

The physiological values of the main time-domain metrics are reported in Table 2.2. It should be noted that these values are approximate, and can be influenced by age, sex and recording duration [11, 27].

Table 2.2: Approximate physiological values of selected time-domain HRV metrics in healthy adults.

Metric	Typical value
$\overline{NN}$	600–1000 ms
SDNN	~30–80 ms
RMSSD	~20–70 ms
pNN50	>3% (means 5–20 %)
SD1	~20–50 ms
SD2	~50–150 ms

2.1.4.2 Frequency-domain metrics

Frequency-domain HRV analysis characterizes the distribution of power across different frequency bands by applying spectral estimation techniques to the NN interval time series. Common methods include the Fast Fourier Transform (FFT) and parametric approaches, which offer improved frequency resolution for short data segments.
The principal spectral contributions arise from the very-low-frequency (VLF, < 0.04 Hz), low-frequency (LF, 0.04–0.15 Hz), and high-frequency (HF, 0.15–0.40 Hz) bands. HF power predominantly reflects parasympathetic activity linked to respiration, whereas LF power represents a mixture of sympathetic and parasympathetic influences mediated largely by baroreflex mechanisms, rather than purely sympathetic activity [28, 29]. The VLF band contributes minimally in short-term recordings and remains physiologically less well understood; therefore, it is often excluded from the analysis of short ECG segments. Additionally, the LF/HF ratio is often reported as an index of the relative balance between low and high-frequency components of HRV.
Frequency-domain metrics are commonly expressed in absolute units (ms^2) or normalized units, which emphasize the relative contributions of LF and HF components and facilitate inter-subject comparisons. These methodological considerations and their physiological interpretation are emphasized in established HRV measurement standards [11, 25].

The main time and frequency-domain metrics are summarized in Table 2.3.

Table 2.3: Main HRV metrics in the time and frequency-domain.

Metric	Unit	Description	Physiological meaning
Time-domain			
NN (or $\overline{NN}$)	ms	Mean normal-to-normal interval	
SDNN	ms	Standard deviation of NN intervals	Overall variability
RMSSD	ms	Root mean square of successive differences	Short-term variability
pNN50	%	% of successive NN differences > 50 ms	
SD1	ms	Poincaré width	Short-term variability
SD2	ms	Poincaré length	Long-term variability
Frequency-domain			
VLF (< 0.04 Hz)	ms^2	Very-low-frequency power	
LF (0.04–0.15 Hz)	ms^2	Low-frequency power	Mixed autonomic/baroreflex
HF (0.15–0.40 Hz)	ms^2	High-frequency power	Respiration/vagal activity
LF/HF	a.u.	Ratio between LF and HF components	Autonomic balance

2.1.5 Respiratory Rate (RR)

Respiratory rate (RR) represents the number of breathing cycles—each consisting of one inspiration and one expiration—occurring per minute. In healthy adults at rest, RR typically ranges from 12 to 20 breaths per minute (bpm) [30], although it varies with metabolic demand, posture, and autonomic regulation.

The act of breathing is governed by rhythmic activity of brainstem respiratory centers, which coordinate the mechanical actions of the diaphragm and thoracic muscles to modulate lung volume. During inspiration, intrathoracic pressure decreases, venous return to the heart increases, and vagal efferent activity transiently withdraws; these effects shorten the beat-to-beat interval, leading to a slight acceleration of HR. Conversely, during expiration, vagal tone increases, venous return decreases, and the beat-to-beat interval lengthens, resulting in a deceleration of HR. This cyclical modulation of cardiac timing by the respiratory cycle is known as respiratory sinus arrhythmia (RSA) [12, 31].

RSA reflects a physiological mechanism by which the parasympathetic nervous system, primarily via the vagus nerve, regulates rapid fluctuations in HR in synchrony with breathing. As such, variations in RR and the coupling between respiration and cardiac activity contribute significantly to high-frequency component of HRV. Importantly, this cardiorespiratory coupling allows researchers to estimate RR from HRV measurements through RSA-based approaches [12, 31].

In addition, cyclic thoracic motion during respiration induces periodic changes in electrode position and orientation with respect to the cardiac electrical sources. During expiration, when the thorax is relatively contracted, electrodes tend to record ECG signals with higher amplitude, whereas during inspiration thoracic expansion is often associated with reduced signal amplitude. These variations in electrode–heart geometry, together with changes in thoracic impedance, result in QRS amplitude modulation over time. The indirect extraction of respiratory information from such ECG amplitude modulations, or through RSA, is commonly called ECG-derived respiration (EDR) [32, 13].

EDR is widely used, as it offers a convenient and sensor-free approach by exploiting respiration-related modulations of the ECG signal, such as QRS amplitude variations and RR interval fluctuations. In addition, its main advantage lies in the ability to extract respiratory content

from ECG recordings without further devices or hardware, making it particularly suitable for long-term and wearable monitoring applications. However, these methods are inherently indirect and their accuracy may be affected by noise, motion artifacts, and significant changes in autonomic regulation. Conversely, direct respiratory sensors—such as impedance pneumography, accelerometers, respiratory belts, or airflow sensors [33]—measure breathing activity directly and generally provide more reliable results under a wide range of conditions. This improved accuracy comes at the cost of increased system complexity, and additional sensors. Consequently, the choice between EDR-based estimation and direct respiratory sensing represents a trade-off between convenience and measurement accuracy.

2.2 Wearable Devices for Physiological Monitoring

2.2.1 Opportunities

Recent advances in wearable sensing technologies have enabled continuous and unobtrusive monitoring of physiological signals in both fitness and healthcare applications. Devices such as smartwatches, chest patches, wristbands, and smart garments are increasingly used to acquire cardiorespiratory signals including HR, HRV [34], and RR. Compared to traditional clinical instrumentation, wearable devices offer greater convenience, portability, and reduced cost, making them suitable for large-scale and long-term monitoring [35, 36].
A key advantage of wearable systems lies in their ability to support continuous and longitudinal data acquisition, which is particularly relevant for medical conditions characterized by transient, unpredictable, or context-dependent events. In such cases, sporadic in-clinic assessments may fail to capture relevant physiological changes. Continuous monitoring allows for the detection of subtle autonomic alterations that unfold over extended periods, providing access to real-world physiological dynamics that are not observable during short laboratory recordings [35, 36].
From a patient-centered perspective, wearable devices improve comfort and compliance by allowing individuals to maintain their normal daily activities in familiar environments. This ecological validity is especially important when investigating stress-related and functional disorders, where clinical settings may alter autonomic responses. Furthermore, the integration of wearable devices with mobile platforms enables real-time data storage, remote supervision, and scalable deployment, supporting personalized and preventive healthcare approaches.

2.2.2 Limitations and Noise Sources

Despite their considerable potential, wearable devices present important limitations and technical challenges that must be carefully addressed. Compared to clinical-grade systems, wearable sensors are more susceptible to noise and signal degradation due to their operating conditions and simplified hardware. One major source of variability arises from the skin–sensor interface, which can be affected by motion, sweating, electrode placement, and individual skin properties.
In particular, dry electrodes—commonly used in wearable devices for comfort and ease of use—often exhibit higher electrode–skin impedance and lower signal quality than traditional wet or gel-based interfaces [37]. These factors directly impact the signal-to-noise ratio (SNR), which quantifies the relative strength of the physiological signal of interest with respect to unwanted noise components.
A reduced SNR indicates that relevant physiological features—such as cardiac depolarization

waves or respiration-induced modulations—may be partially masked by noise, increasing the likelihood of detection errors and unreliable parameter estimation. In wearable recordings, variations in electrode contact and impedance fluctuations can substantially reduce SNR, particularly during movement, thereby challenging the accurate extraction of cardiorespiratory parameters.
Motion artifacts represent one of the most critical challenges for non-invasive physiological monitoring [38]. Body movements can induce mechanical disturbances at the skin-sensors interface, leading to transient signal distortions that may obscure relevant physiological features, especially in ECG and photoplethysmographic (PPG) recordings. In addition, electromyographic (EMG) interference, originating from skeletal muscle activity, can overlap in frequency content with cardiac signals and significantly affect the reliability of beat detection [9].
These artifact sources are particularly problematic during daily activities, where physical movement and postural changes are unavoidable. As a result, robust signal processing techniques—including artifact detection, noise suppression, and SNR enhancement—are essential to ensure reliable extraction of physiological parameters such as HR, HRV, and RR from wearable data [36]. The main artifact sources and their characteristics are grouped and summarized in Table 2.4 [3, 21]. Understanding these limitations is crucial when interpreting wearable-derived autonomic measures and when designing algorithms suitable for real-world monitoring scenarios.

Table 2.4: Common ECG noise sources and their characteristics.

Noise source	**Features**	**Origin**
Power-line interference (PLI)	Sinusoidal oscillations at 50 Hz or 60 Hz	Coupling with the local main
Baseline wander	Low-frequency fluctuations (typically < 0.5 Hz)	Respiration and slow body movements
Electrode–skin contact noise	Transient distortions or dropouts due to impedance changes	Variations in electrode–skin contact quality (impedance)
Motion artifacts	Transient, high-amplitude distortions	Electrode displacement or mechanical motion during body movements
EMG interference	Spectral components may overlap with ECG signal	Skeletal muscle activity near the recording electrodes
Instrumentation noise	Interference introduced by acquisition electronics	Amplifiers, analog-to-digital converters, and other system components

2.3 Signal Processing for Wearable ECG

2.3.1 Signal Filtering and Artifact Removal

Wearable ECG recordings are generally affected by multiple sources of noise and artifacts that can significantly degrade signal quality. In order to accurately identify ECG morphological features—such as the QRS complex and fiducial points—a robust signal processing pipeline

is essential [10, 39]. Reliable preprocessing is not only critical for clinical assessment of arrhythmias and cardiac diseases [3], but also represents a prerequisite for accurate R-peak detection and subsequent HRV analysis, where even a small number of detection errors may introduce substantial bias in time and frequency-domain HRV metrics.
A fundamental preprocessing step consists of bandpass filtering the ECG signal to isolate frequency components of interest while attenuating noise. The ECG signal exhibits most of its diagnostically relevant spectral content below 40–45 Hz, whereas baseline wander is concentrated at very low frequencies (typically below 0.5 Hz) and muscle artifacts extend toward higher frequencies with significant overlap above 20–30 Hz [21]. In particular, the QRS complex is characterized by a relatively high-frequency content compared to P and T waves, with dominant energy commonly reported between approximately 5 Hz and 15–20 Hz [40]. This spectral separation justifies the widespread use of band-pass filters with cutoff frequencies selected according to the application and noise conditions. Commonly adopted ranges in the literature include 0.5–40 Hz [41] or 1–40 Hz [42] for general ECG preprocessing, and narrower bands such as 5–15 Hz [40] or 8–20 Hz [43] when the primary objective is QRS complex enhancement and robust R-peak detection.
In addition to band-pass filtering, notch filters are frequently employed to suppress narrowband interference while preserving surrounding spectral components. Notch filtering is particularly effective for attenuating PLI at 50 Hz or 60 Hz (depending on the local power grid), which may otherwise distort ECG morphology and compromise feature extraction accuracy [44].
Beyond linear filtering, wearable ECG signals often benefit from advanced artifact removal techniques due to the prevalence of motion artifacts and EMG contamination during daily activities [9]. Median filtering is commonly used to reduce baseline drift and impulsive noise without significantly affecting the QRS morphology, while adaptive filtering techniques dynamically adjust filter parameters to track time-varying noise characteristics [21, 39]. Wavelet-based denoising methods have also gained prominence, as they allow multiresolution decomposition of the ECG signal and selective attenuation of noise components across different scales [45, 46].
Finally, preprocessing pipelines may include signal normalization steps, especially when inter-subject or inter-session comparisons are required. Normalization mitigates the amplitude variability due to differences in electrode placement, skin properties, or device characteristics, reducing the risk of false positives caused by large-amplitude T waves or false negatives associated with low-amplitude R peaks [21].

Overall, effective signal filtering and artifact removal are essential prerequisites for reliable ECG analysis in wearable systems. By exploiting the known spectral characteristics of ECG components—especially the frequency localization of the QRS complex—preprocessing techniques can substantially improve SNR and enhance the robustness of subsequent detection and feature extraction algorithms in real-world monitoring scenarios.

2.3.2 QRS Detection Methods

After signal filtering and artifact attenuation, the detection of R peaks represents a critical step in ECG signal analysis, as R-peak locations define individual cardiac cycles and constitute the basis for HR and HRV estimation. Errors at this stage can propagate through subsequent processing steps, leading to inaccurate physiological measurements. For this reason, a wide range of QRS detection algorithms has been proposed in the literature, exploiting different enhancement strategies to improve robustness in the presence of noise and morphological

variability.
Broadly, QRS detection methods can be categorized according to the domain in which the ECG signal is processed. Time-domain approaches emphasize the steep slopes and high amplitudes of the QRS complex using operations such as differentiation, nonlinear transformations, and adaptive thresholding [40, 47, 43]. Also template matching—which exploits similarity measures between signal and reference template—operates directly on the ECG waveform in the time-domain [48, 9]. Analytic-signal-based methods, including those derived from the Hilbert transform [43], exploit phase and envelope information to improve peak localization. Time–frequency-domain techniques, most notably wavelet-based methods, decompose the ECG signal into multiple scales to selectively enhance transient QRS components while attenuating noise and baseline fluctuations [49, 50, 9]. Not only wavelet transform can be used for time-frequency analysis of ECG signal, but ECG beat detection based on filter banks (FB) has also been proposed in the literature [51]. In FB-based algorithms, the ECG signal is decomposed into multiple subbands with uniform frequency bandwidths. In some cases, optimal combination of above mentioned approaches has been explored [52].
Each of these techniques presents distinct advantages and limitations, particularly when applied to wearable ECG recordings characterized by low SNR and non-stationary artifacts.

In the following sections, three R-peak detection methods—Pan–Tompkins, Hilbert-transform-based detection, and wavelet-based QRS enhancement—are described, providing the methodological foundation for the algorithm adopted in this work.

2.3.2.1 Pan-Tompkins Algorithm

The Pan–Tompkins algorithm is one of the most widely cited and historically influential methods for real-time QRS detection in ECG signals. Originally proposed for ambulatory monitoring applications in 1985, it combines linear filtering, nonlinear transformations, and adaptive decision rules to achieve robust detection under noisy conditions [40]. Its design emphasizes low computational complexity, making it suitable for real-time and embedded implementations.
The algorithm enhances QRS complexes through a sequence of processing stages. First, the ECG signal is band-pass filtered (5–15 Hz) by cascading low-pass and high-pass filters, a frequency range in which most QRS energy is concentrated [40]. This step attenuates baseline wander, power-line interference, muscle noise, and part of the T-wave interference, thereby improving the SNR.
Next, a discrete-time derivative operator emphasizes the steep slopes characteristic of the QRS complex. Since differentiation enhances high-frequency noise, it is followed by a squaring operation, which accentuates large-amplitude features and ensures positive signal values. The resulting signal is then processed through a moving-window integrator (typically ∼150 ms), approximating the expected QRS duration and providing combined slope and width information.
Detection is performed using adaptive thresholding applied to both the integrated signal and the bandpass-filtered ECG. The algorithm continuously updates signal and noise peak estimates to adapt to changes in morphology and heart rate. Additional logic, including a refractory period (∼200 ms) and a search-back mechanism based on RR interval statistics, reduces false detections and recovers missed beats [40].
Pan and Tompkins reported a detection accuracy of approximately 99.3% on the MIT-BIH Arrhythmia Database [40].

Despite reduced robustness in highly noisy wearable ECG recordings, the algorithm remains a fundamental benchmark for evaluating more advanced QRS detection techniques [43].

2.3.2.2 Hilbert Transform-Based Algorithm

Hilbert transform–based algorithms represent an alternative class of first-derivative QRS detectors that exploit phase information to enhance R-peak localization. This approach was proposed as an extension of derivative-based methods to improve robustness while avoiding excessive signal distortion and manual threshold tuning [43].
The method begins with band-pass filtering of the ECG signal (8–20 Hz) to suppress baseline wander and high-frequency noise while preserving the dominant spectral content of the QRS complex. The filtered signal is then differentiated to emphasize the rapid transitions associated with ventricular depolarization. Although differentiation highlights QRS slopes, it introduces phase distortion and produces zero crossings at R-peak locations, requiring a subsequent rectification stage.
Rectification is achieved via the Hilbert transform, which generates the imaginary component of the analytic signal associated with the differentiated ECG. In the frequency domain, the Hilbert transform acts as an all-pass filter with a ±90° phase shift for positive and negative frequencies, respectively. Consequently, zero crossings in the differentiated signal are converted into local extrema, facilitating peak detection. Unlike higher-order differentiation, the Hilbert transform preserves amplitude information due to its uniform magnitude response, thus avoiding excessive attenuation of relevant components [43].
Detection is performed using an adaptive threshold, typically derived from statistical properties of consecutive signal segments, eliminating the need for empirically tuned patient-specific parameters. A refractory period (~200 ms) and a search-back mechanism are commonly implemented to reduce false detections and refine R-peak localization.
Compared to squaring-based detectors such as Pan–Tompkins, Hilbert transform–based methods are less sensitive to signal polarity and benefit from the odd-phase property of the transform, which promotes consistent peak formation. Arzeno et al. reported detection performance comparable to state-of-the-art derivative-based algorithms on standard ECG databases, with advantages in automatic thresholding and morphological preservation [43]. However, as with other first-derivative-based approaches, performance may degrade in the presence of wide QRS complexes, low-amplitude beats, or low SNR.

2.3.2.3 Wavelet-Based Method

Wavelet-based approaches represent one of the most effective time–frequency strategies for QRS detection, particularly in non-stationary and noisy ECG signals such as those acquired from wearable devices. Unlike purely time-domain methods, the wavelet transform (WT) provides simultaneous localization in time and frequency, enabling selective analysis of transient events—such as the QRS complex—characterized by different spectral content compared to P and T waves [53]. Since noise components and baseline drift occupy distinct frequency bands, appropriate scale selection allows effective separation between physiological waves and artifacts [49, 50].
The QRS complex, characterized by sharp temporal transitions and high-frequency components, generates prominent wavelet coefficients at specific intermediate scales. Li et al. demonstrated that QRS complexes correspond to pairs of local maxima in the modulus of the wavelet transform across scales, a property linked to signal singularities [49]. By analyzing the persistence of these modulus maxima across characteristic scales, their method effectively

discriminates QRS complexes from noise, baseline wander, and high-amplitude P or T waves. Motion artifacts, which tend to produce isolated maxima not following physiologically plausible temporal patterns, can also be rejected. Using this strategy, Li et al. reported QRS detection accuracy above 99.8% on the MIT-BIH Arrhythmia Database [49].
Subsequent developments extended wavelet techniques to full ECG delineation. Martínez et al. proposed a multiscale wavelet-based delineator capable of detecting not only R peaks but also the onsets and offsets of P, QRS, and T waves with high temporal precision and robustness to morphological variability and noise. Sensitivity and positive predictivity values above 99.8% were reported on standard databases [50].

Overall, compared to time-domain and analytic-signal-based detectors, wavelet-based methods offer superior robustness to non-stationary artifacts and inter-beat variability—condition frequently encountered in wearable ECG monitoring. However, this improved robustness comes at the cost of higher computational complexity and the need for careful selection of wavelet functions and analysis scales. Despite these trade-offs, wavelet-based approaches are widely regarded as among the most reliable strategies for QRS detection in challenging recording conditions.

Chapter 3

Materials and Methods

3.1 Experimental Design

This study was designed as a methodological feasibility investigation aimed at developing and evaluating a robust ECG-based signal processing framework for wearable cardiorespiratory monitoring. The primary objective was to implement a complete processing pipeline including ECG denoising, reliable R-peak detection, and extraction of HRV and respiratory parameters during daily activities.

The study was organized into two phases. In the first phase, the signal processing algorithms were developed using ECG recordings acquired from three healthy adult subjects. This dataset was used to design the processing pipeline and preliminary test its performance under controlled conditions.
In the second phase, the robustness of the proposed framework was evaluated under realistic real-life conditions. The evaluation was conducted on one healthy adult subject during both resting-state and dynamic conditions representative of daily activities, intentionally selected to introduce motion-induced artifacts typical of wearable monitoring scenarios.
As an additional aspect of the evaluation phase, the influence of electrode placement was investigated by comparing two wearable adhesive dry patches positioned at different locations on the trunk within the same experimental session.
Given the exploratory nature of the dynamic evaluation phase, conclusions regarding motion robustness are limited to a single-subject feasibility assessment.

3.2 Experimental Setup

3.2.1 Wearable Device

The device used in this study was the P-Cardio HP2011-Lead wearable ECG recorder (2M Engineering, Fig. 3.1), capable of providing high-resolution (24-bit) ECG recordings for long-term monitoring. The system acquires a single-lead ECG signal together with a bioimpedance-based respiration (BioZ) signal and motion data obtained from an inertial measurement unit integrating accelerometer, gyroscope, and magnetometer sensors. A dedicated software application installed on a personal computer enabled real-time visualization of the acquired signals and rapid data download.

Figure 3.1: P-Cardio recorders (50x35x9mm, 20gr).

ECG and bioimpedance-based respiration signals can be configured with sampling rates of 250, 500, or 1000 Hz. In this study, a sampling rate of 250 Hz was selected for both signals. In addition, the device records the state of a push-button integrated on the recorder with sampling rate of 1 Hz. When pressed, the button state is set to "1", otherwise it is set to "0". This feature was used during recordings to mark the beginning and end of specific activities, enabling precise identification of task intervals during post-process signal segmentation.

3.2.2 Electrode Patch and Skin Preparation

The P-Cardio system supports multiple electrode configurations, including reusable wet electrodes, textile-based integrations, and adhesive dry electrode patches. In this study, adhesive dry electrode patches were used for signal acquisition (Fig. 3.2).

Figure 3.2: Dry patch and electrolyte solution.

Prior to the experimental recordings, reusable wet electrodes were temporarily used to verify the correct electrode positioning and signal quality. Subsequently, the subject was instrumented with adhesive dry electrode patches for the data acquisition sessions.
Before electrode placement, the subject's skin was gently abraded and cleaned in order to reduce skin–electrode impedance. A small amount of electrolyte solution was also applied to improve the electrical contact at the electrode–skin interface and ensure stable signal acquisition during the recordings.

3.3 Datasets Description

3.3.1 Development Dataset

The development dataset was used for the design and preliminary testing of the proposed signal processing pipeline. Three healthy adult subjects (two females and one male) were enrolled for this phase of the study. For each participant, long-term ECG (Fig. 3.3) and respiratory signals (Fig. 3.4) were acquired using the wearable P-Cardio device, collecting a total of three signals (Table 3.3.1).

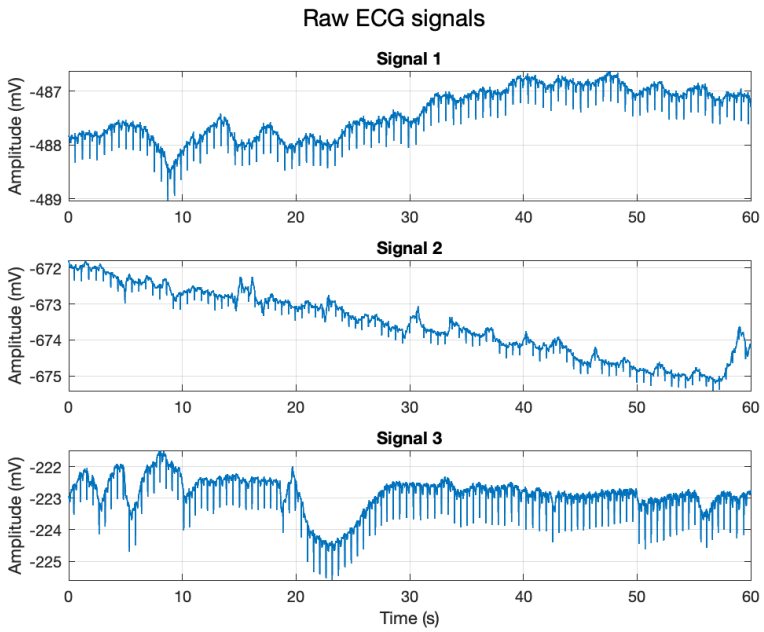

Figure 3.3: Raw ECG signals (1-min window).

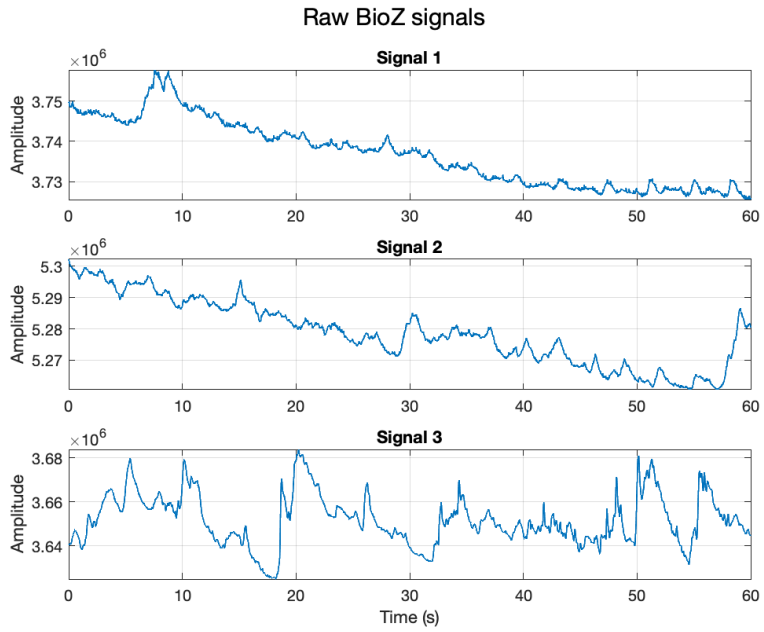

Figure 3.4: Raw BioZ signals (1-min window).

Signal	Duration [min]	Sex	Electrode Patch	Patch Position
1	373	F	Dry	Mid-sternal thoracic
2	285	F	Dry	Mid-sternal thoracic
3	815	M	Dry	Mid-sternal thoracic
Total	**1473**			

Table 3.1: Recording duration with subject characteristic, and patch configuration.

All recordings in this phase were acquired using a single adhesive dry electrode patch positioned in the central thoracic location. These data were used to tune the processing algorithms, including ECG denoising, R-peak detection, and extraction of HRV and respiratory parameters. This step was essential to verify their correct functioning under relatively controlled conditions before evaluating them in more challenging real-life scenarios.

3.3.2 Evaluation Dataset: Daily Activities Dataset

To evaluate the robustness of the proposed framework under non-stationary conditions, a second dataset was acquired during activities of daily living (ADLs). In this phase, one healthy adult subject participated in a long-term monitoring session designed to introduce motion-induced artifacts typical of wearable monitoring scenarios.
ECG and respiratory signals were recorded simultaneously using two identical P-Cardio devices, identified as 3D01 and 3D02. The two devices were connected to adhesive dry electrode patches positioned at different locations on the trunk in order to assess the influence of electrode placement on signal quality. The first patch configuration (3D01) was placed in the mid-sternal thoracic region (Fig. 3.5), whereas the second patch configuration (3D02) was positioned on the left side trunk (Fig. 3.6).

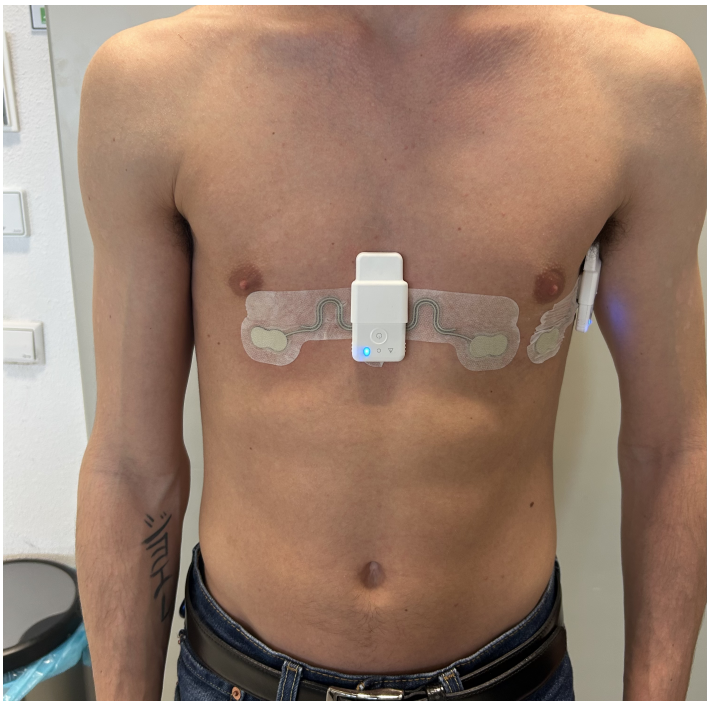

Figure 3.5: Patch configuration: mid-sternal thoracic region (3D01).

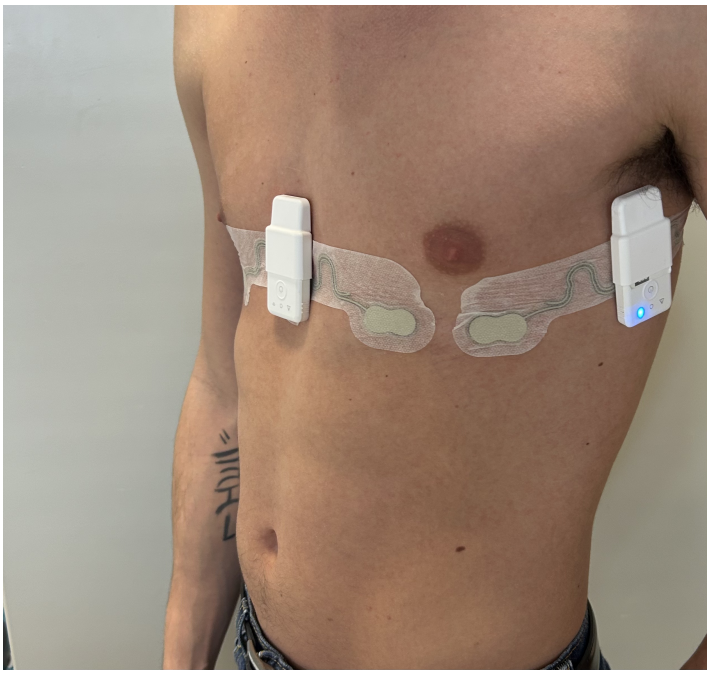

Figure 3.6: Patch configuration: left side trunk (3D02).

During the recording session, the subject was asked to perform multiple motion-based tasks representative of daily activities, including walking at a normal speed, stair climbing, and jumping. In particular, during the jumping task, the subject was instructed to jump for 1 minute followed by 30 seconds of rest, repeated four times consecutively for each jumping session.

3.3.2.1 ADL Dataset Processing

After downloading the raw long-term recordings, signal segmentation was performed to extract the task intervals from the continuous data. As described in Section 3.2.1 button state recorded by the device was used to identify the beginning and the end of each task. Specifically, signal samples between the first occurrence of a "1" and the subsequent "1" in the button state were segmented.
After identifying each task interval, the signal segments were normalized to obtain trials of the same length across the two devices for subsequent comparison. It should be noted that resting-state and sleeping trials were extracted directly from the continuous recordings without marker-based segmentation. Since these segments were predefined with the same duration, the normalization procedure was not required.

Following the segmentation and normalization procedures, the resulting dataset consisted of multiple trials corresponding to the performed daily activities. A summary of the extracted trials and their corresponding durations is reported below in Table 3.2.

Table 3.2: ADL dataset structure.

Activity	**Number of trials**	**Total duration [min]**
Resting-state	138	690
Sleeping	176	880
Walking	8	114
Stair climbing	6	31
Jumping	5	30
Total		**1745**

Some examples of extracted ECG (Figures 3.7-3.8) and respiratory signals (Figures 3.9-3.10) are illustrated below.

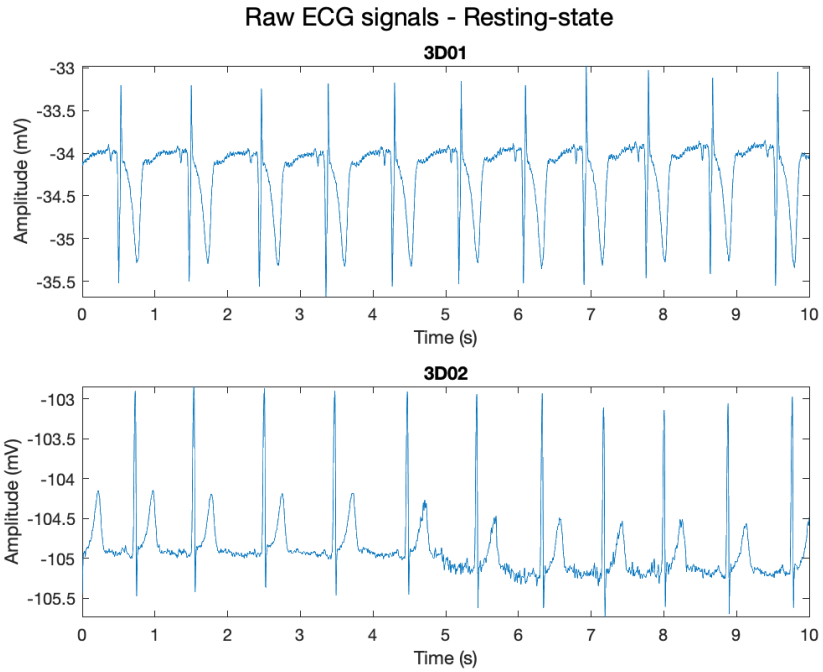

Figure 3.7: Portion of raw ECG signal during resting-state (trial n.8) for both patch configurations (3D01 and 3D02). The difference in polarity between the two signals can be observed.

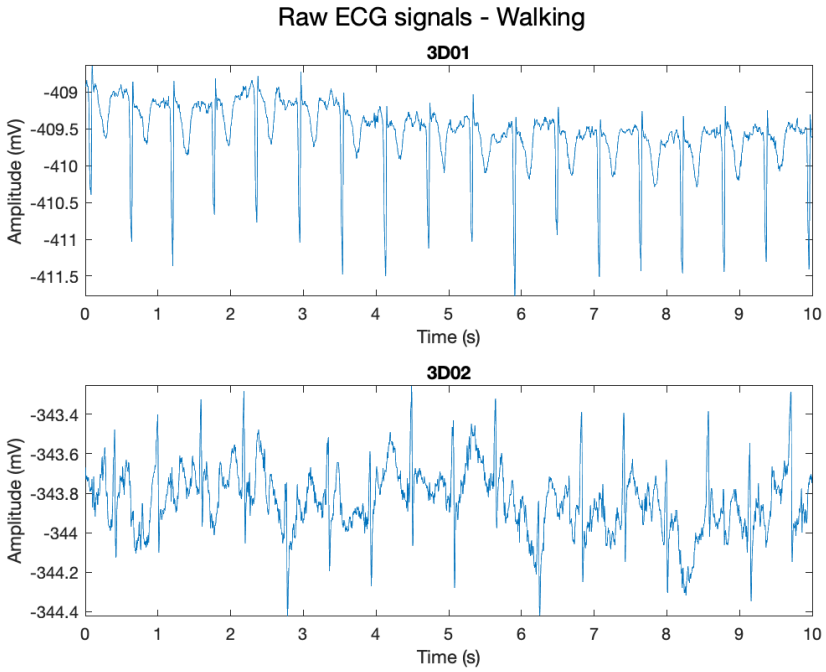

Figure 3.8: Portion of raw ECG signal during walking (trial n.8) for both patch configurations (3D01 and 3D02).

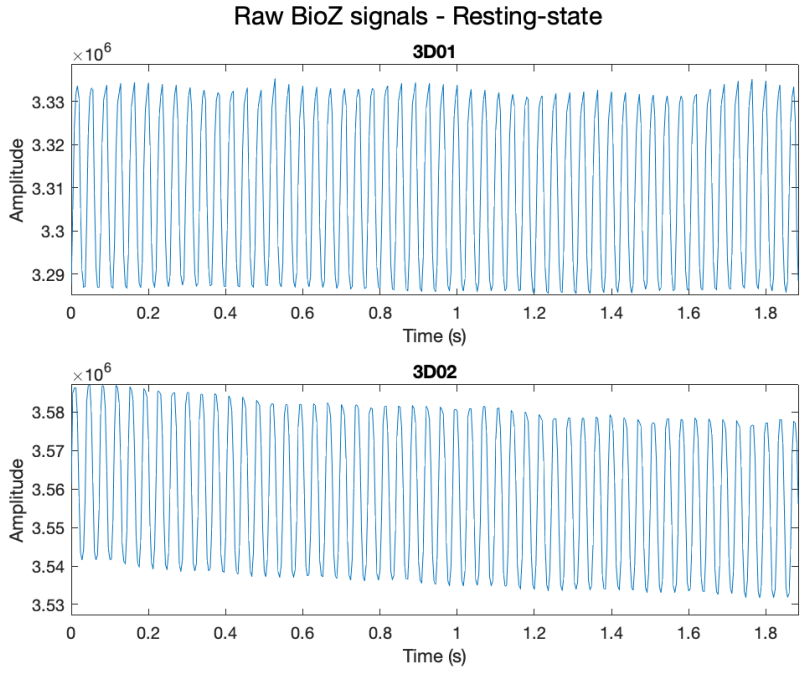

Figure 3.9: Portion of raw BioZ signal during resting-state (trial n.8) for both patch configurations (3D01 and 3D02).

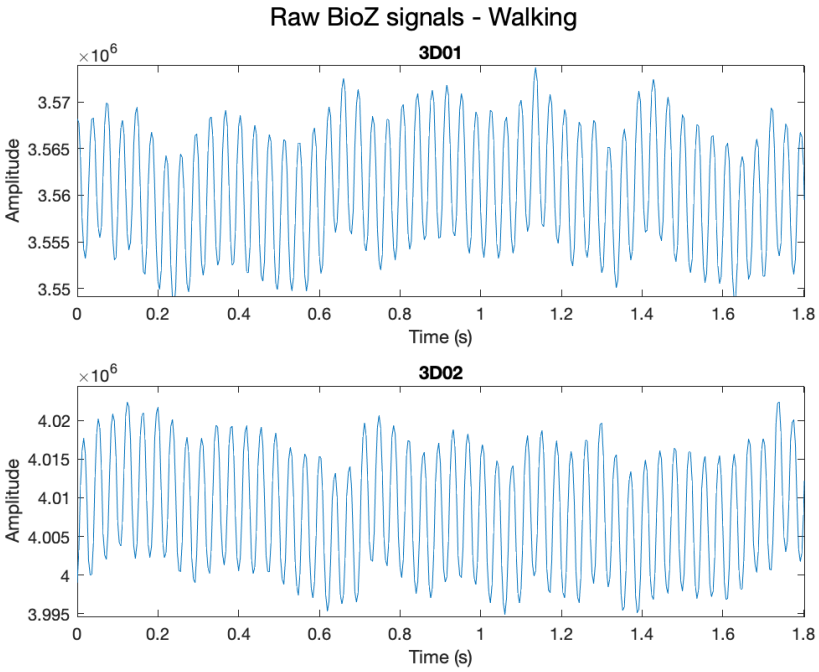

Figure 3.10: Portion of raw BioZ signal during walking (trial n.8) for both patch configurations (3D01 and 3D02).

3.4 Signal Processing Pipeline

To provide an overview of the proposed signal processing pipeline, Fig. 3.11 illustrates the main stages implemented. Starting from the raw ECG and respiratory signals, the pipeline includes bandpass filtering, R-peak detection, beat-to-beat interval computation, HR and HRV metrics extraction, and respiratory rate estimation.

The entire framework was implemented in MATLAB (The MathWorks, Natick, MA, USA).

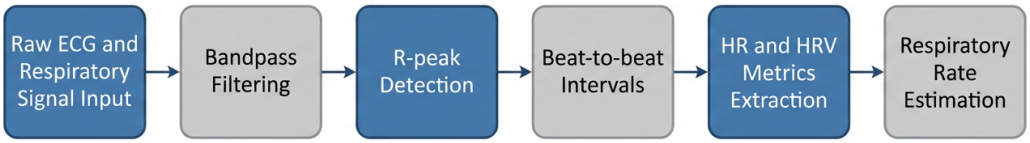

Figure 3.11: Workflow of the proposed signal processing pipeline.

3.4.1 Signal Filtering and R-Peak Detection

In this section, the three different signal filtering strategies and R-peak detection methods evaluated during the development phase of the signal processing pipeline are described.

3.4.1.1 Pan-Tompkins Algorithm

This method consists of sequential processing stages designed to enhance ventricular depolarization components and suppress noise.

According to Pan and Tompkins [40], the implemented procedure can be described as follows:

1. **Bandpass Filtering**
   The signal was first bandpass filtered using a 4th-order Butterworth filter with cutoff frequencies of 5–15 Hz (Fig. 3.12) to emphasize the dominant spectral components of the QRS complex. The filter was applied using zero-phase forward-backward filtering (MATLAB *filtfilt* function) to avoid phase distortion.

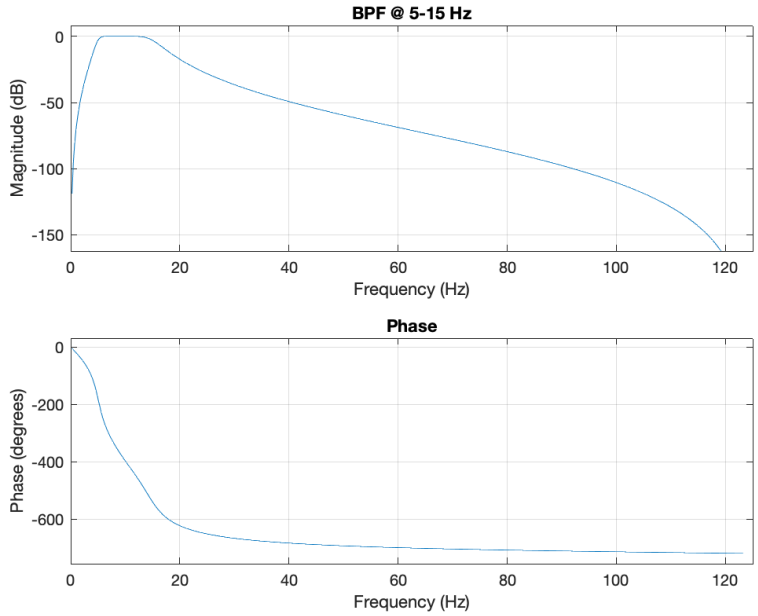

Figure 3.12: Magnitude and frequency response of the 4th-order Butterworth bandpass filter (5–15 Hz).

2. **Derivative Operator**
   Following bandpass filtering, a discrete derivative operator was applied to highlight rapid slope variations characteristic of ventricular depolarization.

3. **Squaring Operator**
   The differentiated signal was squared to:

   - enhance high-amplitude components;
   - suppress low-amplitude fluctuations;
   - ensure positivity of the signal.

4. **Moving Window Integration (MWI)**
   A moving average window of approximately 150 ms was applied to obtain an energy envelope of the QRS complex, consistent with its physiological duration.

5. **Candidate Peak Detection**
   The local maxima were identified on the integrated signal using a minimum peak distance of 200 ms to prevent physiologically incorrect detections.

6. **Adaptive Thresholding**
   The signal and noise levels were estimated from the first two seconds of valid recording and continuously updated during processing.
   Two adaptive thresholds were used:

   - one applied to the integrated signal;
   - one applied to the bandpass-filtered ECG signal for confirmation.

7. **Additional Decision Criterions**
   Additional mechanisms were implemented to improve robustness:

- T-wave discrimination based on slope comparison to avoid misclassification;
- Search-back mechanism to recover missed beats when RR intervals exceeded 1.66 times the estimated average RR interval.

8. **Peak Detection**
   The final R-peak locations were identified on the bandpass-filtered ECG signal (Fig. 3.13).

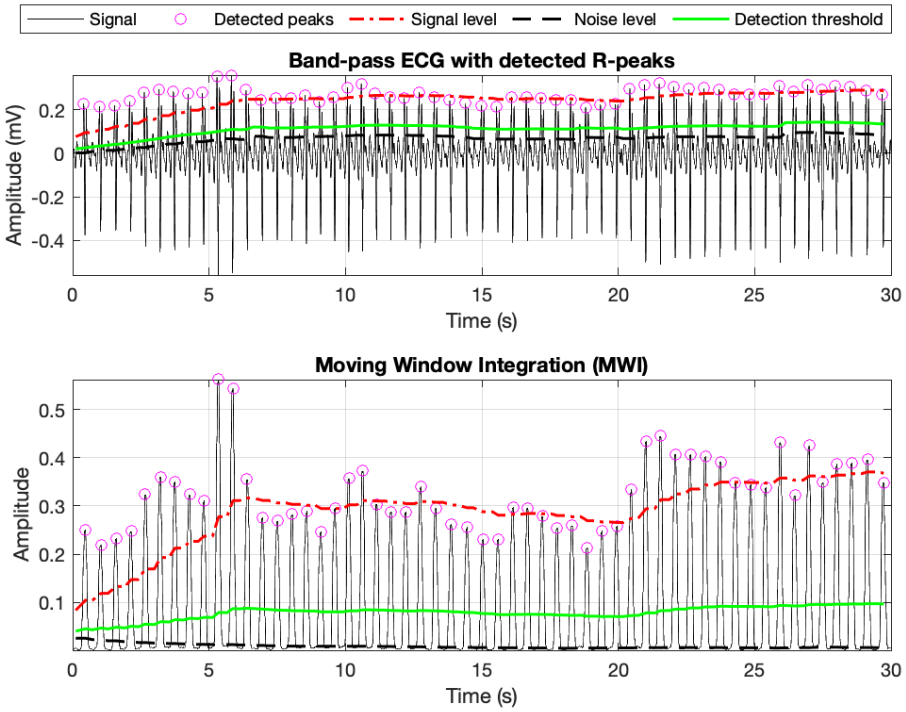

Figure 3.13: Pan-Tompkins detection algorithm: band-pass ECG with detected R-peaks, MWI and thresholds.

3.4.1.2 Hilbert Transform-Based Algorithm

The Hilbert transform-based QRS detector was implemented as an alternative time-domain approach to Pan-Tompkins algorithm. This method enhances the QRS complex by combining derivative filtering with analytic signal representation and adaptive thresholding.

According to Arzeno et Al. [43], the implemented procedure can be described as follows:

1. **Bandpass Filtering**
   The signal was first bandpass filtered using a 4th-order Butterworth filter with cutoff frequencies of 8–20 Hz (Fig. 3.14) to emphasize the dominant spectral components of the QRS complex. The filter was applied using zero-phase forward-backward filtering (MATLAB *filtfilt* function) to avoid phase distortion.

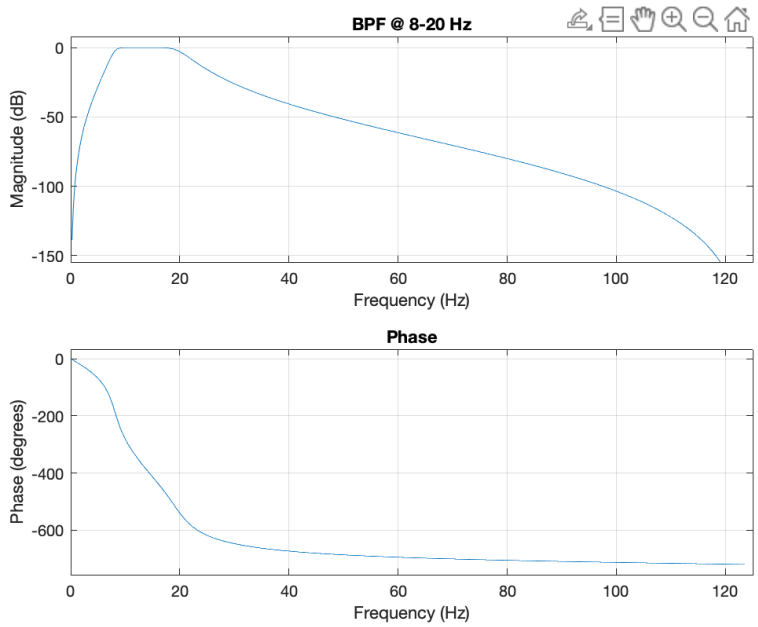

Figure 3.14: Magnitude and frequency response of the 4th-order Butterworth bandpass filter (8–20 Hz).

2. **Derivative Operator**
   Following bandpass filtering, a three-point non-causal central derivative was applied to enhance rapid slope variations associated with ventricular depolarization:

$$d[n] = \frac{x[n+1] - x[n-1]}{2} \tag{3.1}$$

3. **Hilbert Transform of the Derivative**
   The imaginary part of the analytic signal of the derivative was computed using the Hilbert transform:

$$h[n] = \mathrm{Im}\,\{\mathcal{H}\{d[n]\}\} \tag{3.2}$$

   This transformation enhances phase-related characteristics of the QRS complex and emphasizes positive deflections without taking the absolute value, maintaining polarity sensitivity.

4. **Adaptive Thresholding**
   The signal was processed in windows of 1024 samples. For each window:

   - the maximum value and RMS was computed;
   - an adaptive threshold was determined based on the relationship between window maximum and RMS.

5. **Candidate Peak Detection**
   Positive peaks above the adaptive threshold were detected using a physiological refractory constraint of 200 ms to prevent multiple detections within a single cardiac cycle.

6. **Search-Back Mechanism**
   If the RR interval exceeded 1.5 times the previous RR interval, a secondary search was performed within the expected interval to identify potentially missed beats. A reduced threshold (90% of the current threshold) was used during this recovery stage.

7. **Peak Refinement**
   For each detected candidate, the precise R-peak location was refined by searching within a ±10-sample window on the bandpass-filtered ECG signal (Fig. 3.15).

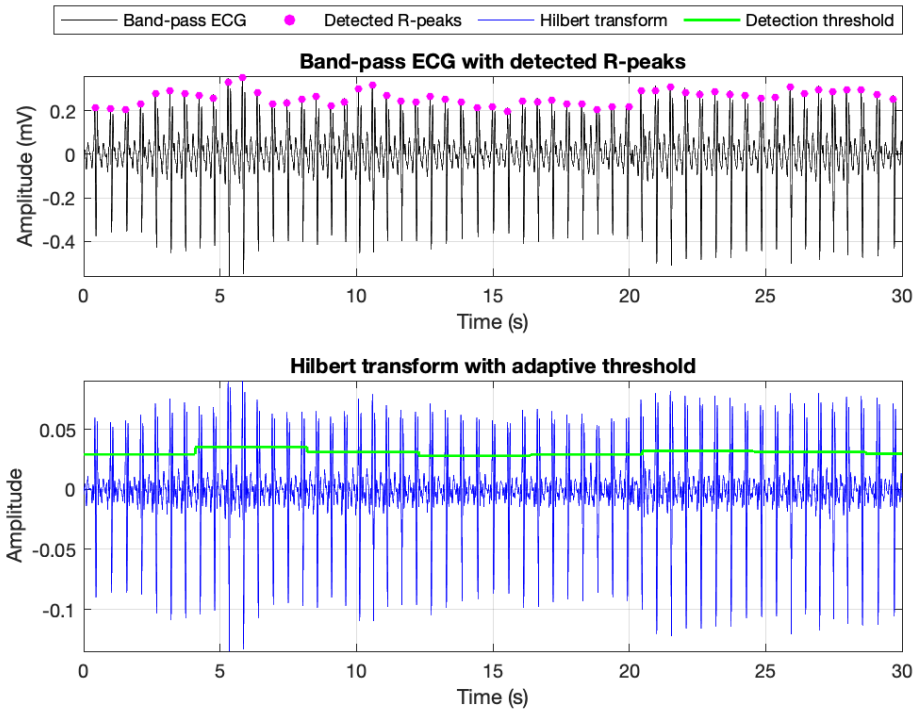

Figure 3.15: Hilbert transform-based detection algorithm: band-pass ECG with detected R-peaks and Hilbert transform.

3.4.1.3 CWT-Based Method

A continuous wavelet transform (CWT)-based approach was also implemented to improve robustness against motion artifacts and background noise. The method enhances QRS-related time–frequency components and detects R-peak candidates on an envelope obtained by combining multiple wavelet scales.

The implemented procedure can be described as follows:

1. **Bandpass Filtering**
   First, bandpass filtering was performed using a 4th-order Butterworth filter with cutoff frequencies of 5–40 Hz (Fig. 3.16). In contrast with filters employed for Pan-Tompkins and Hilbert-based methods, the broader band used for the CWT-based approach was chosen to preserve a wider portion of QRS complex, which is beneficial for multi-scale wavelet analysis [48, 49, 50]. The filter was applied using zero-phase forward-backward filtering (MATLAB *filtfilt* function) to avoid phase distortion.

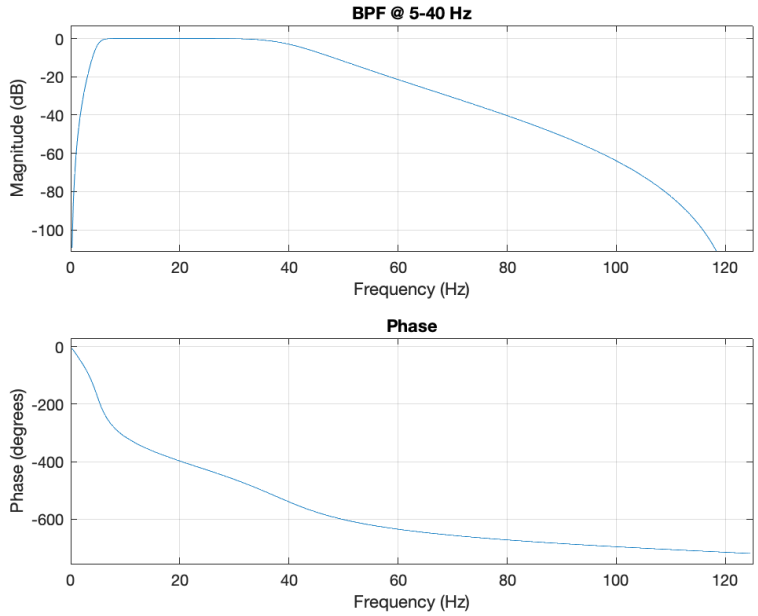

Figure 3.16: Magnitude and frequency response of the 4th-order Butterworth bandpass filter (5–40 Hz).

Some examples of bandpass filtered ECG signals during resting-state (Fig. 3.17) and walking (Fig. 3.18) conditions are illustrated below.

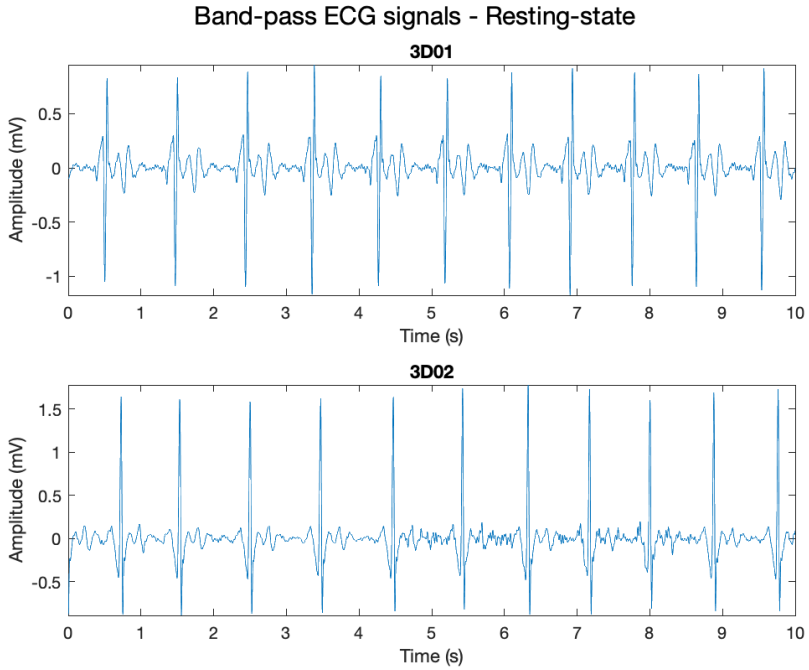

Figure 3.17: Portion of bandpass filtered ECG signal during resting-state (trial n.8) for both patch configurations (3D01 and 3D02).

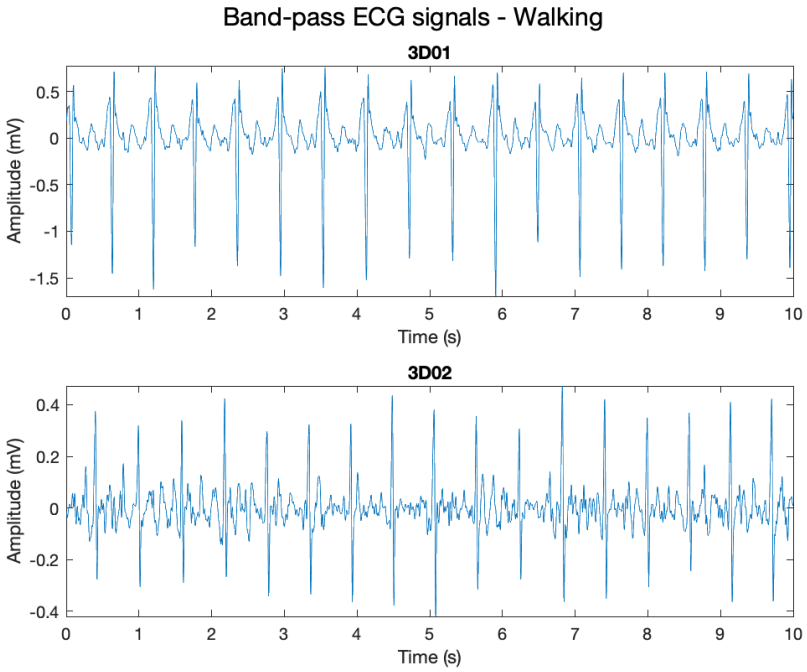

Figure 3.18: Portion of bandpass filtered ECG signal during walking (trial n.8) for both patch configurations (3D01 and 3D02).

2. **Continuous Wavelet Transform (CWT)**
   Following bandpass filtering, the CWT of the signal:

$$W_x(a,b) = \int_{-\infty}^{+\infty} x(t)\,\frac{1}{\sqrt{a}}\,\psi^*\left(\frac{t-b}{a}\right)\,dt \tag{3.3}$$

   was computed using the analytic Morlet wavelet (MATLAB *amor*) within a frequency range selected to emphasize QRS content:

   - $a \in \mathbb{R} \setminus \{0\}$ is the *scale* parameter, $b \in \mathbb{R}$ is the *translation* parameter, and $\psi(t)$ is the mother wavelet.
   - Frequency limits: 15–40 Hz.

3. **Multi-Scale Combination**
   The wavelet coefficients within the selected frequency range were combined by summing their magnitudes across scales, producing an enhanced envelope. The resulting signal was then normalized to the range [0,1].

4. **Candidate Peak Detection**
   The R-peak candidates were detected using MATLAB *findpeaks* function on the enhanced envelope, enforcing:

   - Minimum peak distance: 200 ms as physiological refractory constraint;
   - Minimum peak height: 82nd percentile of the envelope values as adaptive amplitude criterion.

5. **Peak Refinement**
   Each detected candidate was refined by searching within a ±40 ms window on the band-pass filtered ECG signal (Fig. 3.19).

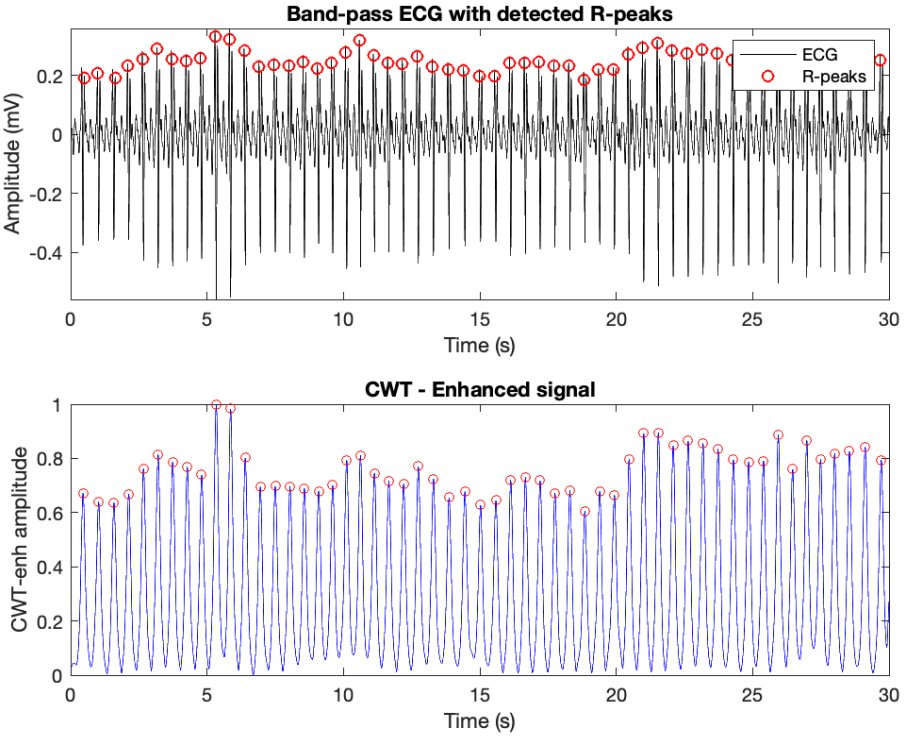

Figure 3.19: CWT-based detection algorithm: band-pass ECG with detected R-peaks and CWT-enhanced signal.

Some examples of ECG signals with detected R-peaks during resting-state (Fig. 3.20) and walking (Fig. 3.21) conditions are illustrated below.

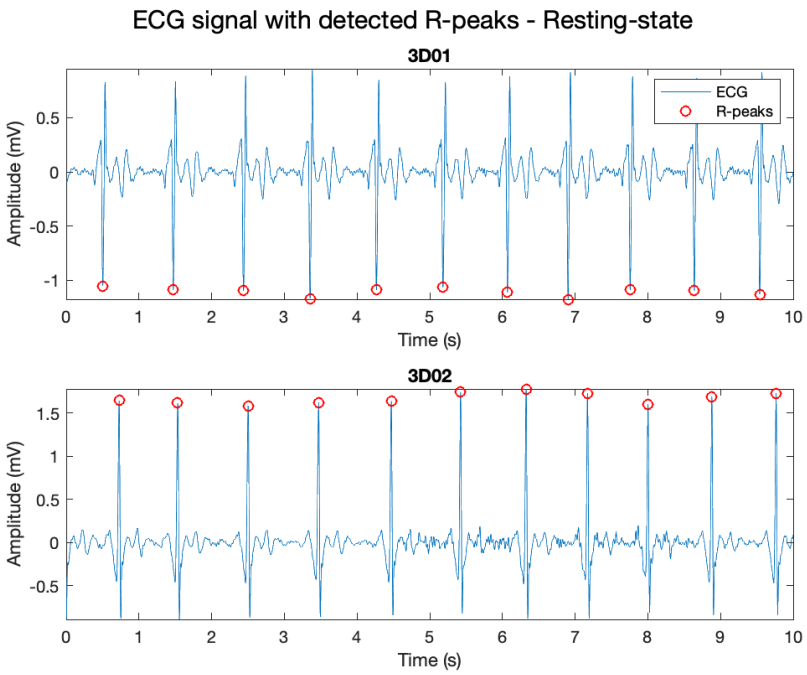

Figure 3.20: Portion of ECG signal with detected R-peaks during resting-state (trial n.8) for both patch configurations (3D01 and 3D02).

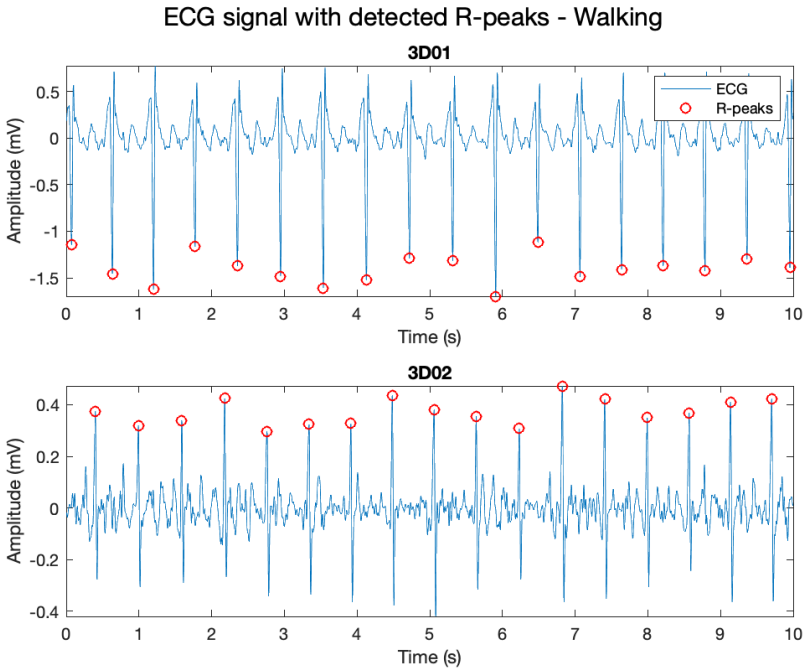

Figure 3.21: Portion of ECG signal with detected R-peaks during walking (trial n.8) for both patch configurations (3D01 and 3D02).

Given the fixed electrode configuration, R-wave polarity was consistent across recordings for each device. Therefore, R-peak refinement for each method was performed by selecting the local extremum (maximum or minimum, depending on device polarity). Finally, the corresponding temporal positions were obtained by dividing the sample indices by the sampling

frequency.

Based on the comparative evaluation of these three implemented R-peak detection methods (described in Section 4.1.2), the CWT-based approach was selected for integration into the final signal processing pipeline and the 5–40 Hz bandpass filtering was consequently adopted.

3.4.2 HR and HRV Metrics Extraction

In this section, the procedure performed for HRV metrics extraction is described. After R-peak detection using the CWT-based method, R-peak locations were identified for each trial. RR series (beat-to-beat intervals) were then computed as the difference between consecutive R-peak temporal positions.
Given the relatively short duration of each trial, the RR series were segmented into 1-minute windows (Figures 3.22-3.23), and HRV metrics were computed for each window. This approach allowed the extraction of a sufficient number of HRV estimates for each trial.

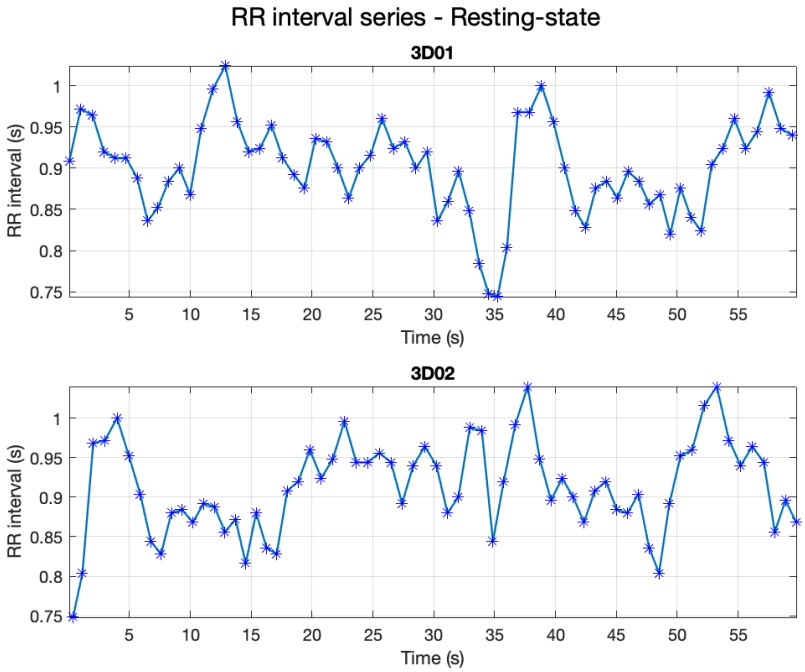

Figure 3.22: 1-min window of beat-to-beat intervals during resting-state (trial n.8) for both patch configurations (3D01 and 3D02).

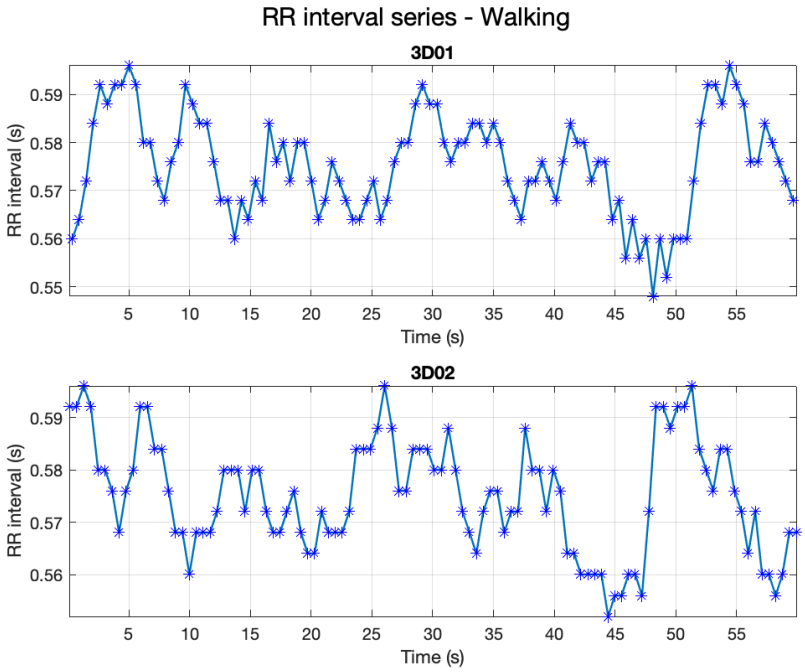

Figure 3.23: 1-min window of beat-to-beat intervals during walking (trial n.8) for both patch configurations (3D01 and 3D02).

Due to the use of 1-minute windows, only time-domain HRV metrics were calculated. Frequency-domain metrics were intentionally excluded, as 1-minute segments are insufficient for reliable estimation of VLF, LF, and HF spectral components.

3.4.2.1 Time-Domain Metrics

For each 1-minute RR interval segment, the following time-domain HRV metrics were computed:

- **Mean Heart Rate ($\overline{HR}$)**
  HR provides an overall measure of cardiac activity during the analyzed interval. Mean HR was calculated as:

$$\overline{HR} = \frac{60}{\overline{RR}} \tag{3.4}$$

  where $\overline{RR}$ represents the mean RR interval expressed in seconds.

- **SDNN (Standard Deviation of NN Intervals)**
  SDNN reflects overall HRV and represents the total variability within the analyzed time window. SDNN was calculated as:

$$SDNN = \sqrt{\frac{1}{N-1}\sum_{i=1}^{N}\left(RR_i - \overline{RR}\right)^2} \tag{3.5}$$

  where RR_i denotes individual beat-to-beat intervals and N is the number of beats in the segment.

- **RMSSD (Root Mean Square of Successive Differences)**
  RMSSD quantifies short-term beat-to-beat variability and is primarily associated with vagal modulation. RMSSD was calculated as:

$$RMSSD = \sqrt{\frac{1}{N-1}\sum_{i=1}^{N-1}(RR_{i+1} - RR_i)^2} \tag{3.6}$$

- **pNN50**
  pNN50 represents the percentage of successive RR interval differences greater than 50 ms and is commonly used as an index of short-term HRV. Similar to RMSSD, this metric mainly reflects parasympathetic modulation of heart rate. pNN50 was calculated as:

$$pNN50 = \frac{1}{N-1}\sum_{i=1}^{N-1} I\left(|RR_{i+1} - RR_i| > 50\,\text{ms}\right) \times 100 \tag{3.7}$$

  where RR_i and RR_{i+1} represent two consecutive RR intervals, N is the number of beats in the analyzed segment, and $I(\cdot)$ is an indicator function equal to 1 when the condition is satisfied and 0 otherwise.

3.4.2.2 HRV Metrics Aggregation and Comparison

After computing HRV metrics for each 1-minute RR interval segment, multiple HRV estimates were obtained for each trial. To facilitate interpretation and comparison of the results, two levels of analysis were considered.

At the trial level, HRV metrics computed across the 1-minute windows within each trial were summarized by reporting the mean and the standard deviation. This approach allowed for comparison between the different trials for each activity.

At the activity level, the summarized metrics obtained from individual trials were further grouped according to the type of activity (resting-state, sleeping, walking, stair climbing, and jumping) in order to characterize each condition, by reporting the mean and the standard deviation as well.

3.4.3 Respiratory Rate Estimation

In this section, the methodological approach implemented to extract respiratory rate (RR) from both direct bioimpedance measurement and from ECG-derived respiration (EDR) signal is described.

3.4.3.1 Bioimpedance-Derived Estimation

RR was estimated from the bioimpedance signal through the following processing steps:

1. **Sliding-Window Segmentation**
   Each trial was segmented using a sliding-window approach, with non-overlapping windows of 60 seconds. For each window, the corresponding segment of the bioimpedance-based signal was extracted.

2. **Bandpass Filtering**
   Each segment was bandpass filtered using a third-order Butterworth filter with cutoff frequencies of 0.2–0.4 Hz [32] to isolate the respiratory component (Fig. 3.24). This frequency range corresponds to typical adult respiratory frequencies [30]. The filter was applied using zero-phase forward-backward filtering (MATLAB *filtfilt* function) to avoid phase distortion.

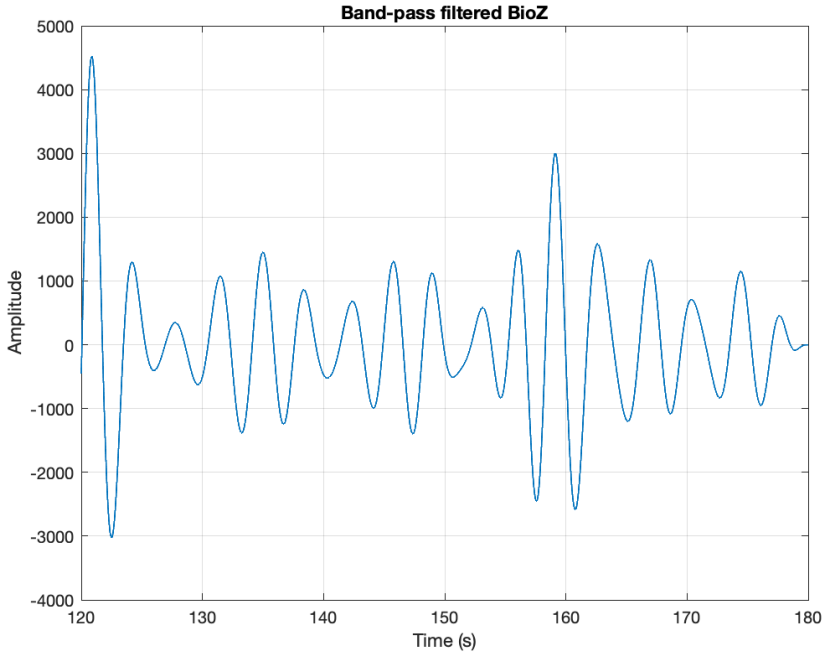

Figure 3.24: Example of 1-min window band-pass filtered bioimpedance-based signal (BioZ).

3. **Respiratory Rate Estimation**
   RR was estimated in the frequency domain by computing the PSD using Welch's method (20 s window, 50% overlap). The dominant frequency within the 0.2–0.4 Hz band was selected and converted to breaths per minute (bpm) by multiplying by 60.

3.4.3.2 Singular Value Decomposition (SVD)

In addition to bandpass filtering, a Singular Value Decomposition (SVD) approach was implemented in this work. SVD was used to perform ECG denoising and to improve Q-wave localization for subsequent QRS amplitude modulation analysis (described in Section 3.4.3.3). Specifically, this method exploits the quasi-periodic structure of the QRS complexes by constructing an aligned beat matrix and performing low-rank approximation.

According to Galli et Al. [54], the implemented procedure can be described as follows:

1. **R-Peak Detection**
   The R-peak locations were first identified using the CWT-based method (see Section 3.4.1.3). These locations were used to segment individual cardiac cycles.

2. **Construction of QRS Matrix**
   For each detected beat, a window centered around the R-peak was extracted. The window

length was set equal to the median RR interval to ensure consistent beat representation. Each segmented beat was aligned with respect to the R-peak and arranged column-wise to form a QRS matrix (Fig. 3.25):

$$X \in \mathbb{R}^{L \times M} \tag{3.8}$$

where:

- L is the number of samples per beat (median cycle length);
- M is the number of detected beats.

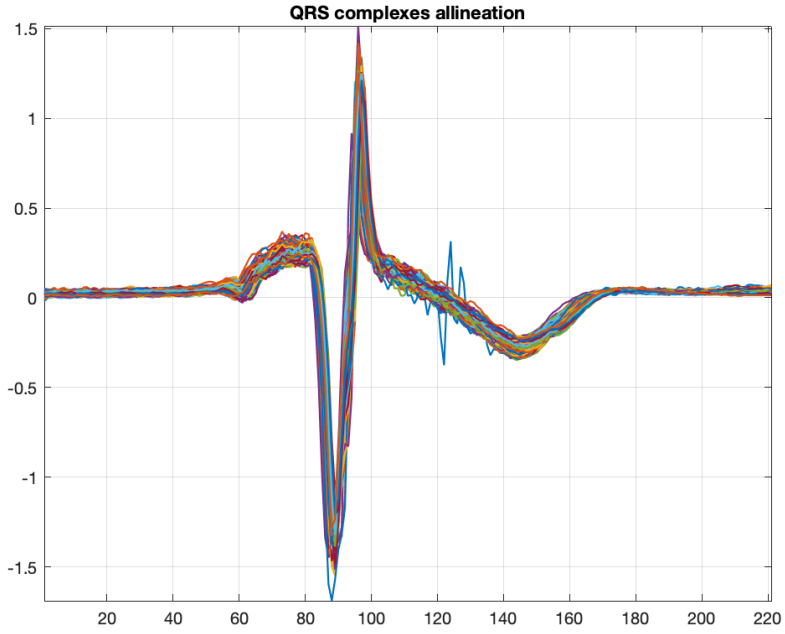

Figure 3.25: Example of QRS complexes allineation (n = 345). A noisier QRS complex in blue can be observed.

3. **Singular Value Decomposition**
   The QRS matrix was decomposed using SVD:

$$X = U\Sigma V^T \tag{3.9}$$

   where:

   - U contains the left singular vectors;
   - Σ is a diagonal matrix of singular values;
   - V contains the right singular vectors.

4. **Selection of Significant Singular Values**
   The number of retained singular values (SVs) N was determined as the value minimizing the reconstruction error while preserving QRS morphology. The Mean Absolute

Percentage Error (MAPE) of the reconstructed QRS amplitude was calculated as follows:

$$\text{MAPE}(N) = \frac{100}{M} \sum_{i=1}^{M} \left| \frac{A_i - \hat{A}_i^{(N)}}{A_i} \right| \tag{3.10}$$

where:

- A_i is the original QRS amplitude of the i-th beat;
- $\hat{A}_i^{(N)}$ is the reconstructed QRS amplitude using the first N SVs.

Table 3.3: MAPE values obtained for different numbers of retained SVs.

Number of SVs (N)	MAPE [%]
2	2.81
3	**2.57**
4	2.38
5	2.42
6	1.84

As shown in Table 3.3, N = 3 was selected as it provides the best trade-off between low MAPE (below 3% for all tested configurations) and effective signal denoising. Retaining a higher number of SVs would reduce the ability to separate signal and noise without achieving a meaningful reduction in the estimation error.

5. **Signal Reconstruction**
   A denoised approximation of the QRS matrix was obtained using only the first N:

$$X_N = U_N \Sigma_N V_N^T \tag{3.11}$$

where:

- U_N contains the first N left singular vectors;
- Σ_N contains the first N SVs;
- V_N^T contains the first N right singular vectors.

The reconstructed beats were then reassembled into a continuous ECG signal, resulting in a smoothed representation with reduced background noise.

3.4.3.3 ECG-Derived Estimation

Compared to the bioimpedance-derived estimation, indirect RR estimation from the ECG signal—based on QRS amplitude modulation—required additional processing stages. The procedure started with the processing of ECG trials. The following steps were performed:

1. **Bandpass Filtering**
   A broad bandpass filtering was performed using a 4-th order Butterworth filter with cutoff frequencies of 1–100 Hz to remove baseline wander. The filter was applied using zero-phase forward-backward filtering (MATLAB *filtfilt* function) to avoid phase distortion.

2. **Denoising with SVD**
   The SVD algorithm (described in Section 3.4.3.2) was employed to obtain a smoother ECG signal (Fig. 3.26), facilitating Q-wave detection. The previously detected R-peak locations were used to construct the QRS matrix.

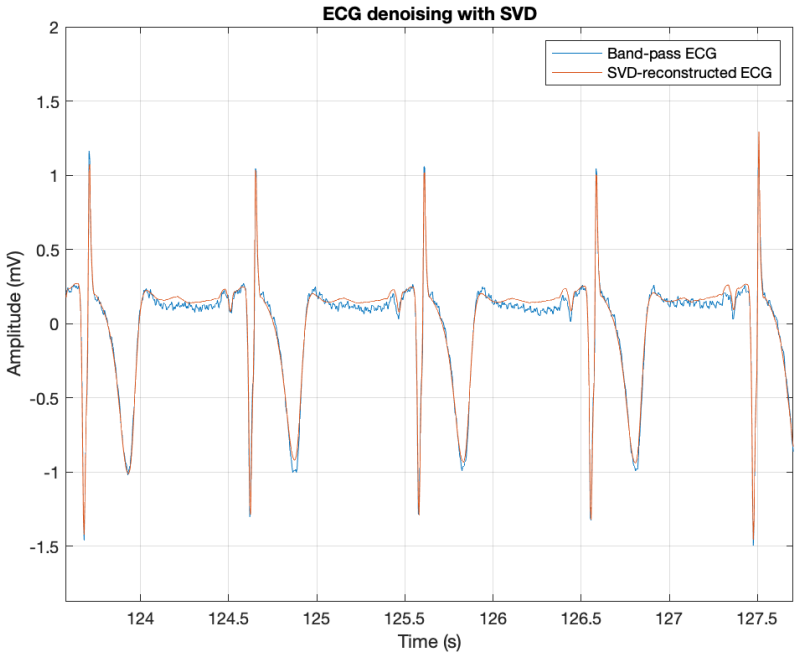

Figure 3.26: SVD denoising: original ECG signal and SVD-reconstructed ECG signal.

3. **Q-Wave Detection**
   First, the CWT-based detection algorithm was applied again to the SVD-reconstructed ECG signal for more accurate R-peak locations. Then, the implemented Q-wave detection algorithm was used to obtain Q-wave locations (Fig. 3.27).
   The Q-wave was identified for each detected R-peak within a 40 ms pre-R window, excluding a 25 ms guard interval immediately preceding the R-peak. Specifically, the dominant slope toward the R-peak was identified, and the Q-wave was then defined as the last zero-crossing of the derivative preceding this slope.

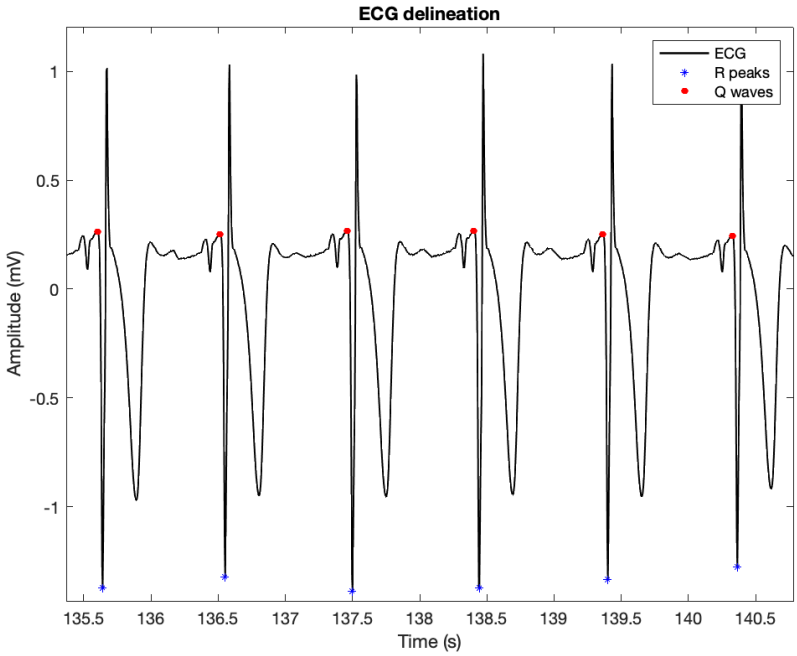

Figure 3.27: ECG delineation: SVD-reconstructed ECG signal with detected R-peaks and Q-waves.

4. **Sliding-Window Segmentation**
   Each task interval was segmented using a sliding-window approach with non-overlapping windows of 60 seconds. For each window, the corresponding R-peak and Q-wave locations were identified.

5. **EDR Signal Construction**
   The ECG-derived respiration (EDR) signal was obtained using the QRS amplitude modulation approach. Specifically, the beat-to-beat QRS amplitude was computed as the absolute difference between the ECG amplitude at the detected R-peak and the corresponding Q-wave. The resulting amplitude series was interpolated using cubic interpolation and resampled at 4 Hz to obtain a uniformly sampled EDR signal.

6. **Bandpass Filtering**
   The EDR signal was bandpass filtered using a second-order Butterworth filter with cutoff frequencies of 0.2–0.4 Hz [32] to isolate the respiratory component (Fig. 3.28). The filter was applied using zero-phase forward-backward filtering (MATLAB *filtfilt* function) to avoid phase distortion.

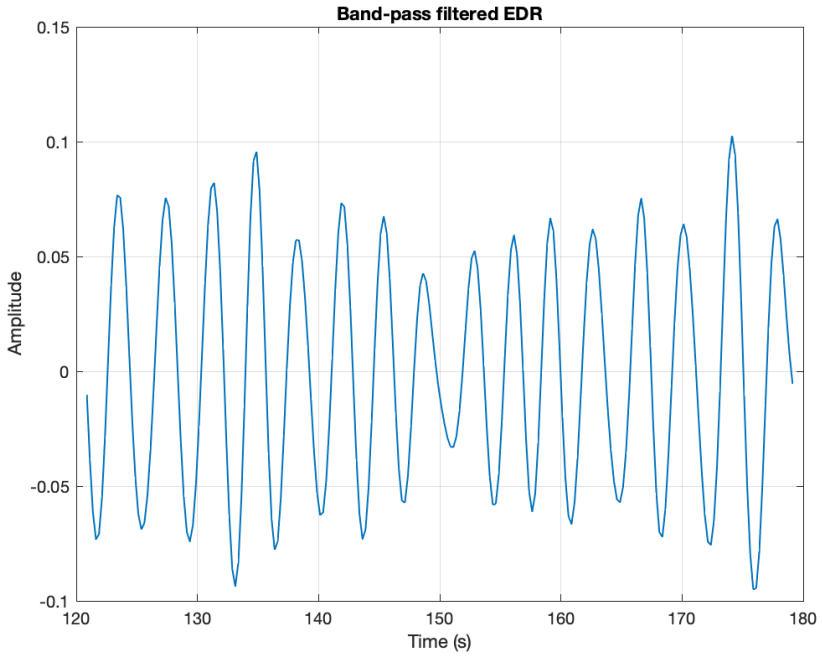

Figure 3.28: Example of 1-min window band-pass filtered ECG-derived respiration (EDR) signal.

7. **Respiratory Rate Estimation**
   RR was estimated in the frequency domain by computing the PSD using Welch's method (20 s window, 50% overlap). The dominant frequency within the 0.2–0.4 Hz band was selected and converted to breaths per minute by multiplying by 60.

3.4.3.4 RR Aggregation and Comparison

Similarly to Section 3.4.2.2, the aggregation procedure was also applied to the RR estimates. After estimating the RR for each 1-minute segment, multiple RR values were obtained for each trial. For result interpretation and comparison, two levels of analysis were considered: trial level analysis, summarizing the RR estimates within each trial, and activity level analysis, averaging trials for each condition. The mean and the standard deviation were reported for each level of analysis.

3.5 Evaluation Criteria

3.5.1 Artifact Detection

To quantify the reliability of the acquired recordings, an artifact detection algorithm was implemented to estimate the proportion of ECG signal effectively usable for the extraction of physiological parameters. The proposed method combines amplitude-based and statistical criteria to identify motion artifacts and abnormal signal distortions.

3.5.1.1 Amplitude Criterion

First, an adaptive amplitude threshold was defined using a moving median envelope of the absolute ECG signal computed over a 60-second window. This long-term envelope was multiplied by a constant threshold factor to obtain a dynamic reference level. A sliding window analysis (0.4 s window with 50% overlap) was then applied to compute the local root mean square (RMS) value of the signal. The RMS value of each window was calculated as:

$$\mathrm{RMS}_w = \sqrt{\frac{1}{N_w}\sum_{i=1}^{N_w} x_i^2} \tag{3.12}$$

where N_w represents the number of samples in the selected window and x_i the sample of the ECG signal.
If the local RMS exceeded the adaptive threshold, the corresponding segment was marked as corrupted. A short temporal padding (± 0.1 s) was applied around the detected center to ensure the precise detection of high-amplitude artifacts (Fig. 3.29).

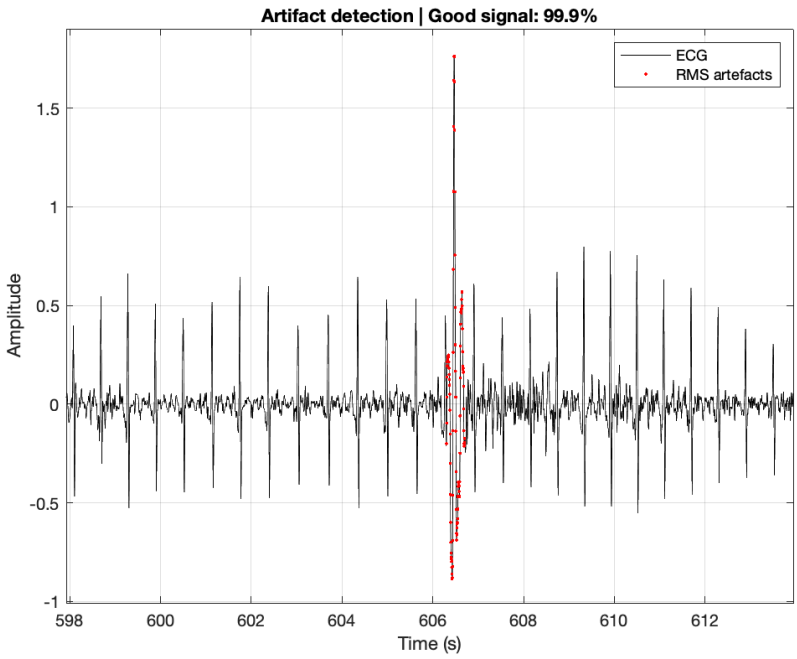

Figure 3.29: Example of high-amplitude artifact.

3.5.1.2 Statistical Criteria

In addition to the amplitude criterion, statistical descriptors were used to identify segments characterized by abnormal morphology. Specifically, kurtosis and spectral entropy were calculated on longer sliding windows (2 s, 50% overlap). Segments with low kurtosis values, indicating flattened signal, or high spectral entropy, reflecting white noise (Fig. 3.30), were classified as corrupted.

Kurtosis was calculated as:

$$\text{Kurtosis} = \frac{1}{N}\sum_{i=1}^{N}\left(\frac{x_i - \mu}{\sigma}\right)^4 \tag{3.13}$$

where μ is the mean value and σ is the standard deviation of the signal x_{i}.

Spectral entropy was computed as the normalized Shannon entropy of the power spectrum:

$$H_{\text{spec}} = -\frac{1}{\log_2(N)}\sum_{k=0}^{N-1} p[k]\log_2(p[k] + \varepsilon) \tag{3.14}$$

where $p[k]$ represents the normalized power spectrum coefficients and N is the segment length. The normalization ensures that:

$$0 \leq H_{\text{spec}} \leq 1 \tag{3.15}$$

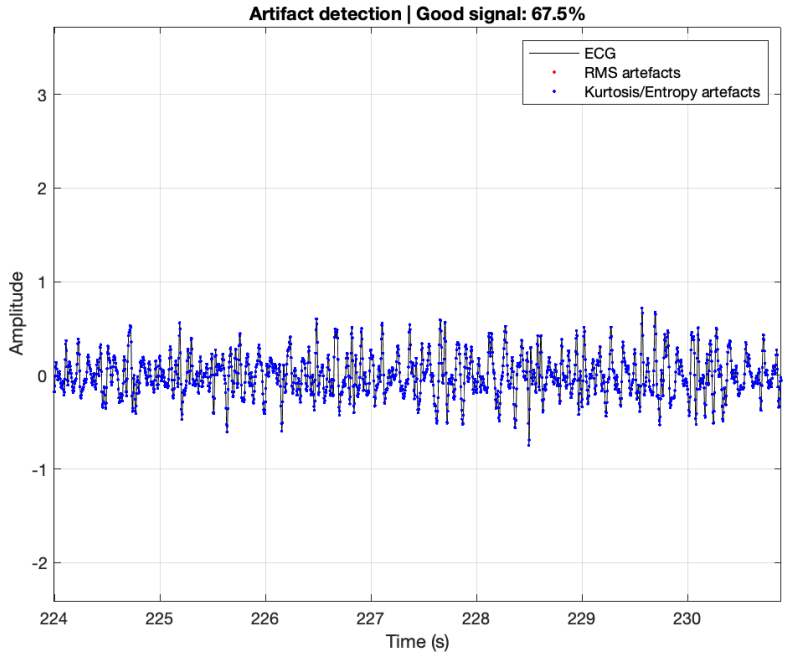

Figure 3.30: Example of high-entropy artifact.

The final artifact mask was obtained by combining amplitude (RMS) and statistical (kurtosis and entropy) detections.
Finally, identified corrupted intervals were used to compute the percentage of usable signal, defined as the ratio between non-corrupted samples and the total number of samples in each segment.

3.5.1.3 Signal Quality Assessment

The implemented artifact detection algorithm was used in two distinct phases. First, it was employed to assess the overall signal quality of the long-term recordings used during the initial

development of the signal processing pipeline (see Section 4.1.1).
Second, the artifact detection algorithm was used to perform a preliminary comparison of signal acquisition reliability during daily activities between the two patch placements. Specifically, as performed with long-term recordings, the algorithm was applied to compute the percentage of usable signal duration within each trial for both devices.
Trials with a usable percentage below 65% were classified as non-reliable and excluded from subsequent analysis, as they were considered too noisy to ensure reliable R-peak detection and accurate parameter extraction. The 65% threshold was empirically determined as a trade-off between ensuring sufficient signal quality for reliable R-peak detection and minimizing unnecessary exclusion of trials.

3.5.2 Valid Beats Percentage

To estimate the percentage of correctly detected beats from the R-peak detection algorithm, three physiological constraints were applied to the RR intervals:

- **Lower bound constraint**: only RR intervals longer than 0.35 seconds (~170 bpm) were considered valid. This avoids non-physiological values due to multiple detections caused by noise and motion artifacts.
- **Upper bound constraint**: only RR intervals shorter than 2 seconds (30 bpm) were considered valid. This excludes non-physiological values due to missed detections.
- $\Delta RR\%$ **constraint**: the relative variation with respect to a 5-beat moving median was required to be below 25%, in order to exclude non-physiological fluctuations due to artifacts or detection errors.

These constraints were necessary because no ground truth annotation was available. Therefore, valid beats were assessed indirectly based on physiological plausibility rather than directly compared with reference annotations. Finally, the percentage of valid beats was calculated as the ratio between valid RR intervals and the total number of RR intervals.

Chapter 4

Results and Discussion

4.1 Development Phase Results

This section contains the results related to the development phase. The quality assessment of the signals used to develop the processing pipeline is first reported. Subsequently, a comparison between three different R-peak detection methods is presented, enabling the selection of the most reliable detector for wearable applications.

4.1.1 Signal Quality Assessment

In this paragraph, the results obtained after signal quality assessment based on amplitude and statistical criteria (see Section 3.5.1) are presented.
Following artifact detection, the effective duration of usable data was quantified for each recording session and reported in Table 4.1.

Signal	Duration [min]	Good Quality [%]	Usable Time [min]
1	373	86.00	320.78
2	285	76.00	216.60
3	815	97.41	793.89
Total	**1473**	**90.40**	**1331.27**

Table 4.1: Recording duration and effective usable time after signal quality assessment.

The results shown in Table 4.1 indicate that the majority of the acquired signal were of sufficient quality to support the development of the proposed processing pipeline. In particular, on average only 10.6% of the total recording duration was classified as non-reliable, allowing a robust preliminary development, based on 1331 minutes of usable ECG and respiratory recordings (i.e., 22 h 11 min). Moreover, the limited amount of discarded data suggests that the acquisition setup provided stable recordings suitable for wearable monitoring.

4.1.2 R-peak Detection Method Comparison

In this section, the results evaluated to select the R-peak detector for the signal processing pipeline are reported. The detection methods were applied only on good-quality signal portions (see Table 4.1) and the percentage of correctly detected R-peaks based on physiological constraints, described in Section 3.5.2.

Table 4.2: Percentage of correctly detected beats for each signal and overall minute-weighted performance.

Signal	**Pan–Tompkins [%]**	**Hilbert-based [%]**	**CWT [%]**
1	84.88	86.75	94.00
2	68.57	72.16	82.04
3	95.58	96.29	98.20
Overall	**88.61**	**90.07**	**94.56**

As shown in Table 4.2, all three detection methods achieved good performance in terms of correctly detected beats, although slightly lower than the values typically reported in the literature [40, 43, 49, 50]. This difference may be attributed to several factors, including the quality of the experimental setup, the consequent signal quality, and the absence of a ground-truth reference for precise validation. In particular, the recordings were obtained with dry electrodes, known for having lower signal quality. Nevertheless, the overall percentage of correctly detected R-peaks was greater than 88% for all the detectors.

Specifically, the CWT-based algorithm achieved the highest overall detection accuracy (94.56%), showing a greater percentage of valid beats compared to the Pan–Tompkins and Hilbert-based approaches. This result suggests that the wavelet-based approach provides improved robustness for wearable ECG applications, likely due to the capability of the WT to isolate the frequency components associated with the QRS complex from background noise and motion artifacts. Based on these observations, the CWT-based method was selected for integration into the final signal processing pipeline.

4.2 Evaluation Phase Results

In this section, the evaluation results obtained during daily activities using the proposed framework are reported. In particular, the analysis focuses on three points: first, the observations related to the patch placement comparison are reported; second, the outcomes of HR and HRV metrics, as well as RR estimation, are presented, providing a comparison across different daily conditions.

4.2.1 Patch Placement Comparison

The results related to the electrode placement comparison are reported below. The comparative assessment focuses on two aspects: the percentage of good-quality signal and the percentage of correctly detected beats. It should be noted that device 3D01 refers to the first patch configuration, while device 3D02 refers to the second patch configuration.

4.2.1.1 Signal Quality Assessment

To evaluate the reliability of the signals acquired by the two patch configurations, the artifact detection procedure was applied for each trial across different daily activities. As an illustrative example, Table 4.3 reports the results obtained for the walking trials. The same evaluation process was then performed for all activities. Importantly, values below 65% are highlighted in red and the corresponding trials were entirely excluded from subsequent analyses.

Table 4.3: Percentage of good-quality signal for walking trials recorded by first patch configuration (3D01) and second patch configuration (3D02).

Walking		
Trial	**3D01 [%]**	**3D02 [%]**
1	100	46.84
2	100	35.84
3	100	57.70
4	100	38.46
5	100	59.44
6	99.99	99.93
7	100	99.17
8	100	100

As shown in Table 4.3, a remarkable difference in the percentage of good-quality signal emerges between the two patch configurations during walking. In fact, most of the walking trials recorded by device 3D02 show percentages below 65%, whereas the percentage for device 3D01 remains consistently close to 100% for all trials.

To further illustrate the artifact detection process, two representative examples are reported below: one segment discarded due to poor signal quality (Figures 4.1a-4.1b) and one segment classified as reliable (Fig. 4.2c), both recorded by device 3D02.

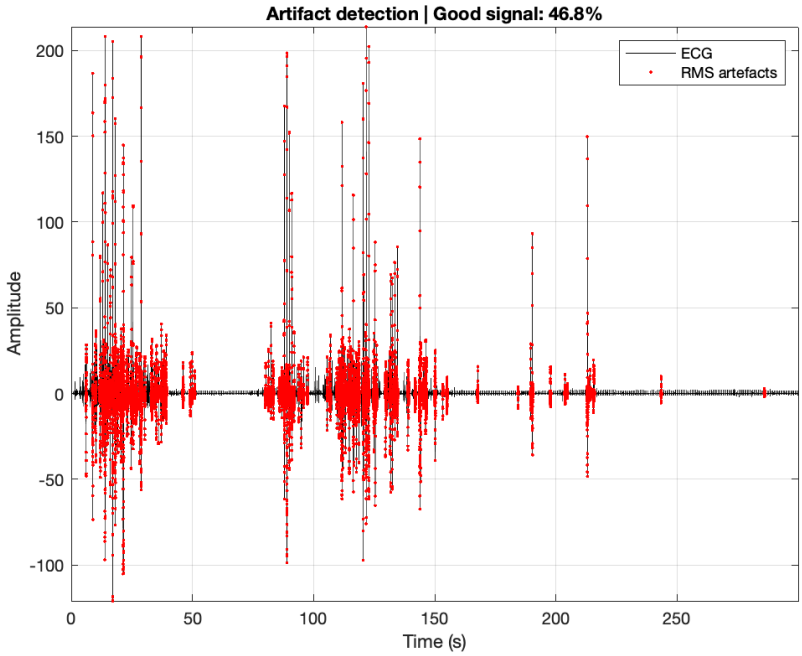
Artifact detection | Good signal: 46.8%
ECG
RMS artefacts
Amplitude
Time (s)
200
150
100
50
0
-50
-100
0
50
100
150
200
250

(a)

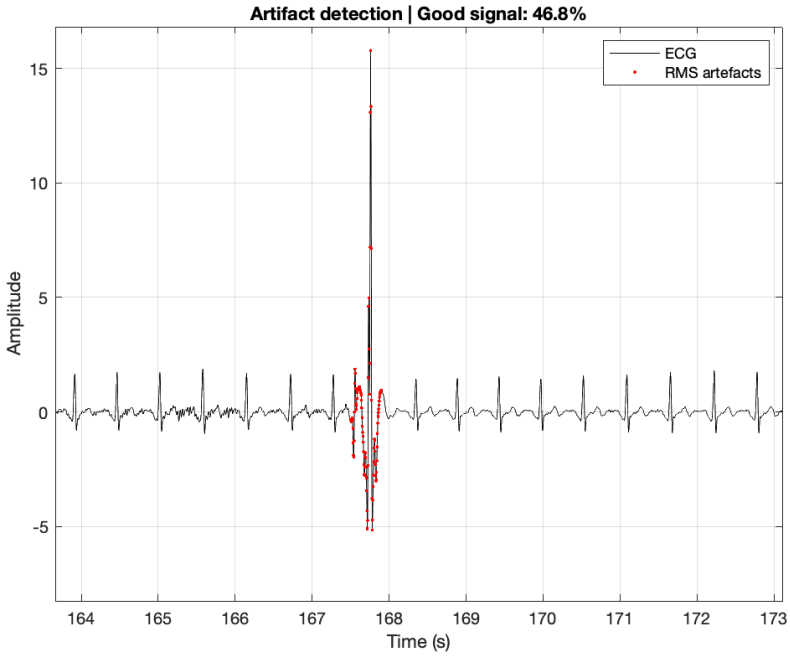
Artifact detection | Good signal: 46.8%
ECG
RMS artefacts
Amplitude
Time (s)
15
10
5
0
-5
164
165
166
167
168
169
170
171
172
173

(b)

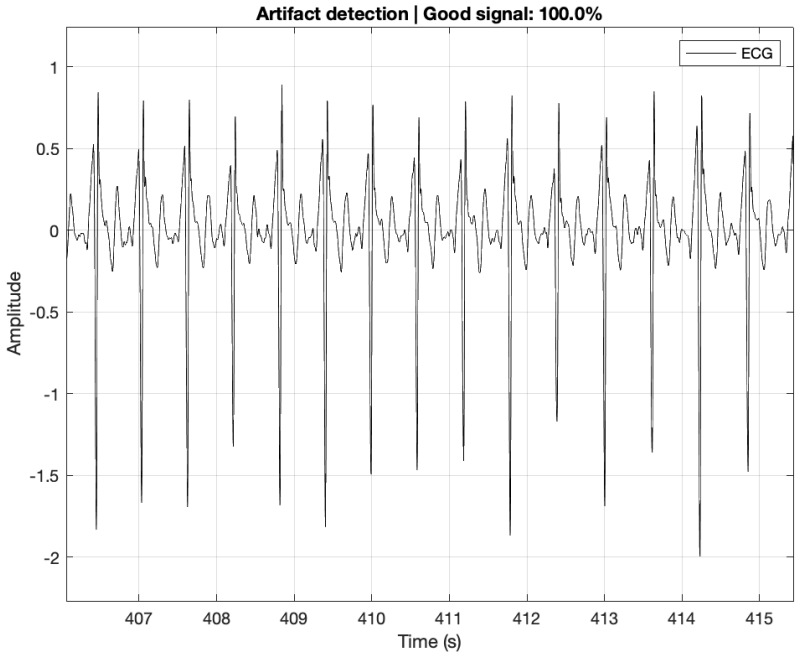

(c)

Figure 4.2: Examples of retained and discarded segments. (a) Resting-state trial n.7 (discarded). (b) Zoom of the discarded trial, highlighting the presence of an amplitude artifact. (c) Zoom of the walking trial n.8 (not discarded).

As illustrated in Fig. 4.2, reliable trials show a clear ECG morphology with stable amplitude, whereas discarded trials show abnormal amplitude fluctuations caused by motion artifacts. These examples highlight how the implemented artifact detection algorithm is capable of correctly distinguishing usable signal portions from corrupted segments.

To provide a comprehensive overview of signal quality across the different activities, Table 4.4 summarizes the percentage of usable signal and the number of discarded trials for each activity and patch configuration. Specifically, these percentages were computed as the ratio between the duration of good-quality signal and the total recording duration for each activity (see Table 3.2). Trials with less than 65% of good-quality signal were entirely discarded, while for the remaining trials the usable duration was weighted according to their respective percentage of valid signal.

Table 4.4: Percentage of usable signal and number of discarded trials across activities for the two patch configurations (3D01 and 3D02).

Activity	**3D01**		**3D02**	
	Usable [%]	**Discarded**	**Usable [%]**	**Discarded**
Resting-state	99.98	0/138	94.36	5/138
Sleeping	99.68	0/176	88.83	18/176
Walking	100	0/8	40.84	5/8
Stair climbing	100	0/6	37.05	4/6
Jumping	100	0/5	19.59	4/5

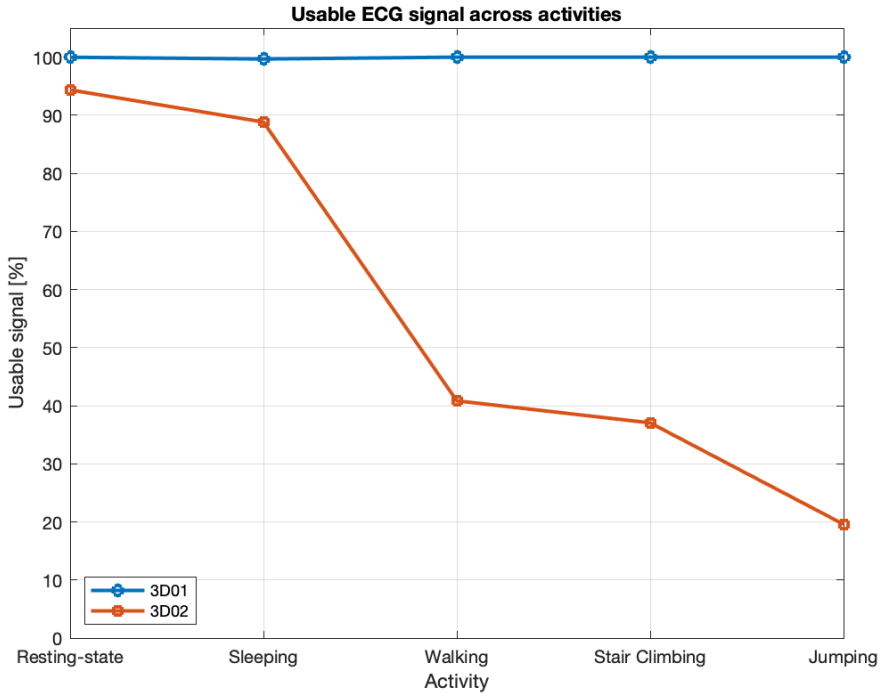

Figure 4.3: Percentage of usable signal across different activities for the two patch configurations (3D01 and 3D02).

From Table 4.4 and Fig. 4.3, it can be observed that the first patch placement (3D01) maintains nearly 100% usable signal across all conditions, and no trials were discarded. This trend indicates a robust acquisition configuration, even during movements.
In contrast, the second patch placement (3D02) shows a progressive degradation in signal quality as the activity becomes more dynamic, dropping from approximately 94% during resting-state to about 20% during jumping. While the number of discarded trials remains low during resting-state and sleeping conditions, a relatively large number of segments were discarded for walking, stair climbing, and jumping.
Considering the second patch positioning, the decrease in usable signal observed during sleeping with respect to the resting-state condition was likely caused by involuntary body movements during sleep, which produced motion artifacts and consequently affected the signal quality.

Overall, these results indicate that the second patch configuration is more susceptible to motion artifacts, probably caused by mechanical interaction with the arm, especially during movement. In contrast, the first patch configuration provides substantially more stable recordings across all conditions.

4.2.1.2 R-peak Detection Performance

The performance of the CWT-based algorithm was then evaluated for the two patch configurations across the different daily activities. The analysis focuses on the percentage of correctly detected beats computed only for retained trials.
As an illustrative example, Table 4.5 reports the percentage of correctly detected beats for the walking trials.

Table 4.5: Percentage of correctly detected beats for walking trials recorded by the first patch configuration (3D01) and the second patch configuration (3D02).

Walking		
Trial	**3D01 [%]**	**3D02 [%]**
1	100	-
2	100	-
3	99.92	-
4	99.08	-
5	99.64	-
6	100	99.06
7	99.62	99.70
8	100	99.35

As shown in Table 4.5, the CWT-based detector achieves very high detection accuracy for device 3D01 across all walking trials, with values consistently close to 100%. For device 3D02, valid detection results are available only for the trials that were not discarded in the previous stage. In these cases, the detector also shows high accuracy, with percentages above 99%.

To provide a global overview of the detector performance across all activities, Table 4.6 summarizes the percentage of correctly detected R-peaks for each condition, referred to the corresponding processed signal duration.

Table 4.6: Percentage of correctly detected R-peaks and corresponding processed signal duration for each activity and patch configuration (3D01 and 3D02).

Activity	**3D01**		**3D02**	
	R-peaks [%]	**Duration [min]**	**R-peaks [%]**	**Duration [min]**
Resting-state	99.93	690	83.41	665
Sleeping	90.34	880	63.90	790
Walking	99.83	114	99.33	47
Stair climbing	99.48	31	99.88	11
Jumping	99.92	30	99.87	6

From Table 4.6, it can be observed that the CWT-based method provides consistently high detection performance for device 3D01 across all activities, with percentages always above 99% except for the sleeping condition, where a slightly lower value (90.34%) is observed.
In contrast, for device 3D02 the detection accuracy is considerably lower during resting-state and sleeping conditions, reaching values of 83.41% and 63.90%, respectively. These results generally reflect the lower signal quality observed for the second patch configuration even in these conditions. For dynamic activities, the detector achieves very high accuracy (above 99%) when applied to the segments that passed the artifact detection stage.
Nevertheless, to better interpret these results, it should be noted that the performance reported for stationary conditions refers to a considerably larger amount of signal, whereas the performance for dynamic activities is computed over a smaller quantity of data. Moreover, the detector performance may be affected by resting-state and sleeping trials characterized by relatively low signal quality, although still above the 65% threshold and therefore not discarded. An illustrative example is reported in Fig. 4.4.

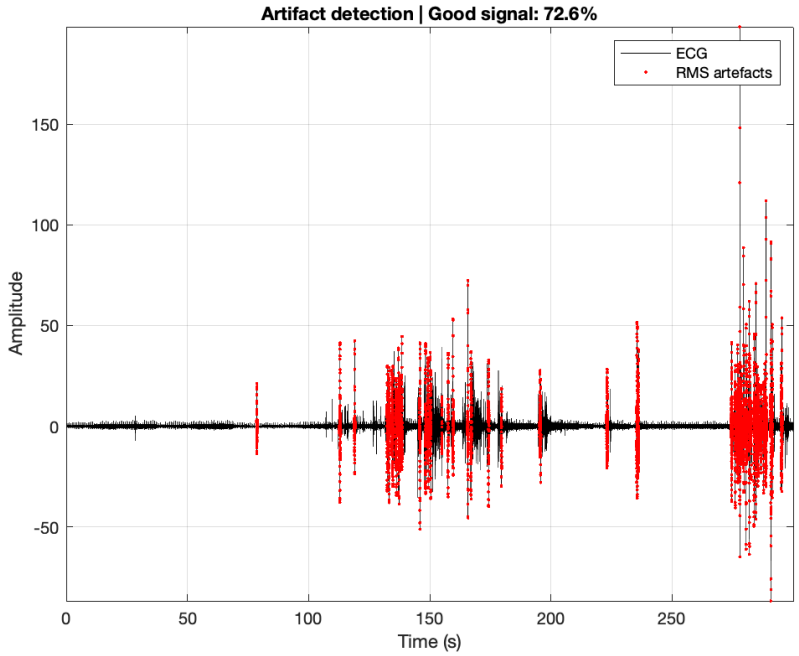

(a)

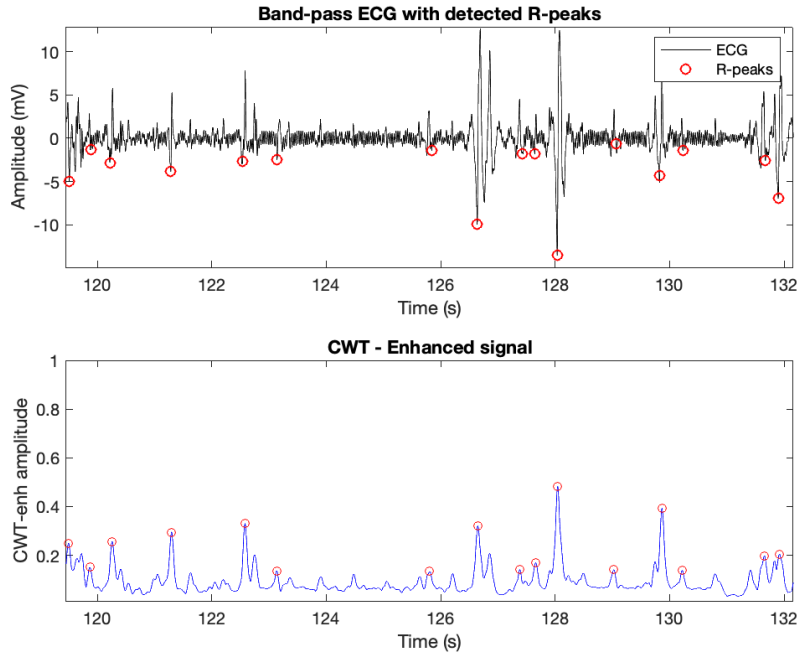

(b)

Figure 4.4: (a) Example of retained trial (resting-state trial n.91) exhibiting percentage of good-quality signal above 65% threshold. (b) CWT-based R-peak detection affected by low signal quality of the retained segment.

In conclusion, the first patch placement ensures both high signal quality and stable detection performance across all activities, whereas the second placement leads to a lower percentage of good-quality signal and reduced detection accuracy in some conditions. These results highlight the impact of patch positioning on the reliability of the ECG signal and, consequently,

on the performance of the R-peak detection algorithm. Based on these observations, the first patch configuration, located in the mid-sternal thoracic region, is better suited for wearable cardiorespiratory monitoring in real-life scenarios.

4.2.2 HR and HRV Metrics

This section presents the results related to HR and HRV metrics extracted using the proposed signal processing pipeline. Due to the limited number of reliable trials available for the second patch configuration, the following analysis focuses on the signals acquired with the first patch placement. As described in Section 3.4.2.2, the results are presented at both trial level and activity level in order to evaluate the consistency of the extracted metrics across different daily activities.

4.2.2.1 Trial Level Results

In this subsection, the HR and HRV metrics estimated for each trial of dynamic activities are reported. The same procedure was implemented also for resting-state and sleeping trials, however the related results were not reported at this level of analysis due to the large number of trials available for these conditions.

Table 4.7: Estimated HR and HRV metrics for trials of dynamic activities (mean ± SD).

(a)

Walking				
Trial	**HR [bpm]**	**SDNN [ms]**	**RMSSD [ms]**	**pNN50 [%]**
1	113.88 ± 4.45	16.08 ± 5.72	10.12 ± 2.05	0.10 ± 0.43
2	98.47 ± 3.01	33.16 ± 12.35	16.97 ± 5.13	2.12 ± 2.83
3	97.31 ± 6.53	46.58 ± 27.45	27.24 ± 13.71	4.53 ± 4.17
4	106.77 ± 2.91	52.80 ± 18.73	53.77 ± 34.65	4.30 ± 2.34
5	118.66 ± 5.86	28.40 ± 26.46	32.94 ± 38.08	1.34 ± 2.31
6	97.79 ± 3.26	28.00 ± 11.30	17.20 ± 7.60	1.99 ± 2.77
7	95.78 ± 5.30	42.83 ± 21.13	23.50 ± 12.63	2.55 ± 2.69
8	104.60 ± 2.81	23.30 ± 15.97	11.77 ± 7.62	1.44 ± 2.74

(b)

Stair climbing				
Trial	**HR [bpm]**	**SDNN [ms]**	**RMSSD [ms]**	**pNN50 [%]**
1	142.87 ± 15.90	38.93 ± 15.11	41.02 ± 27.75	1.43 ± 1.48
2	122.40 ± 16.50	33.75 ± 18.18	21.02 ± 26.16	0.47 ± 0.77
3	123.86 ± 15.04	32.57 ± 28.76	11.13 ± 3.40	0.30 ± 0.47
4	130.50 ± 13.08	28.66 ± 25.57	19.11 ± 27.40	0.29 ± 0.70
5	94.17 ± 2.23	28.98 ± 7.30	16.50 ± 1.86	0.00 ± 0.00
6	112.26 ± 8.96	30.22 ± 12.71	8.89 ± 2.27	0.00 ± 0.00

(c)

Jumping				
Trial	**HR [bpm]**	**SDNN [ms]**	**RMSSD [ms]**	**pNN50 [%]**
1	122.81 ± 8.74	32.19 ± 13.75	14.40 ± 7.87	1.15 ± 1.50
2	122.48 ± 8.34	31.66 ± 15.74	19.71 ± 24.41	0.29 ± 0.71
3	121.99 ± 6.44	29.38 ± 12.80	11.19 ± 2.21	0.42 ± 0.70
4	121.42 ± 3.62	29.14 ± 14.51	10.77 ± 4.71	0.57 ± 0.70
5	131.51 ± 4.38	28.96 ± 25.03	14.04 ± 20.32	0.13 ± 0.32

Table 4.7 summarizes the estimated HR and HRV metrics for each trial of walking, stair climbing, and jumping. Overall, HR values show moderate variability across trials, reflecting differences in effort intensity and individual physiological response during the activities. Regarding HRV metrics, SDNN and RMSSD show pronounced variability between trials and relatively high dispersion as indicated by large standard deviation values. In contrast, pNN50 values remain consistently low across most trials, which is expected during dynamic activities where increased sympathetic activation typically reduces short-term HRV [11, 34].

4.2.2.2 Activity Level Results

In this subsection, a comparison between HR and HRV metrics estimated for each daily activity is reported. Figures 4.5-4.8 reported below illustrate HR, SDNN, RMSSD, and pNN50 values, respectively, across activities.

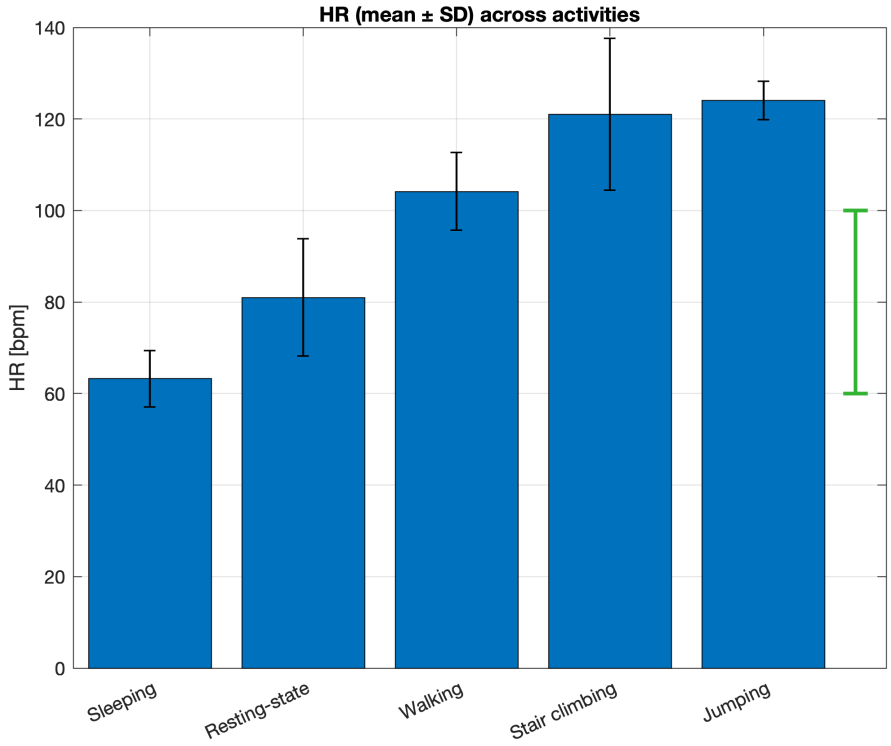

Figure 4.5: HR (mean ± SD) across activities. The green band indicates the physiological range at rest.

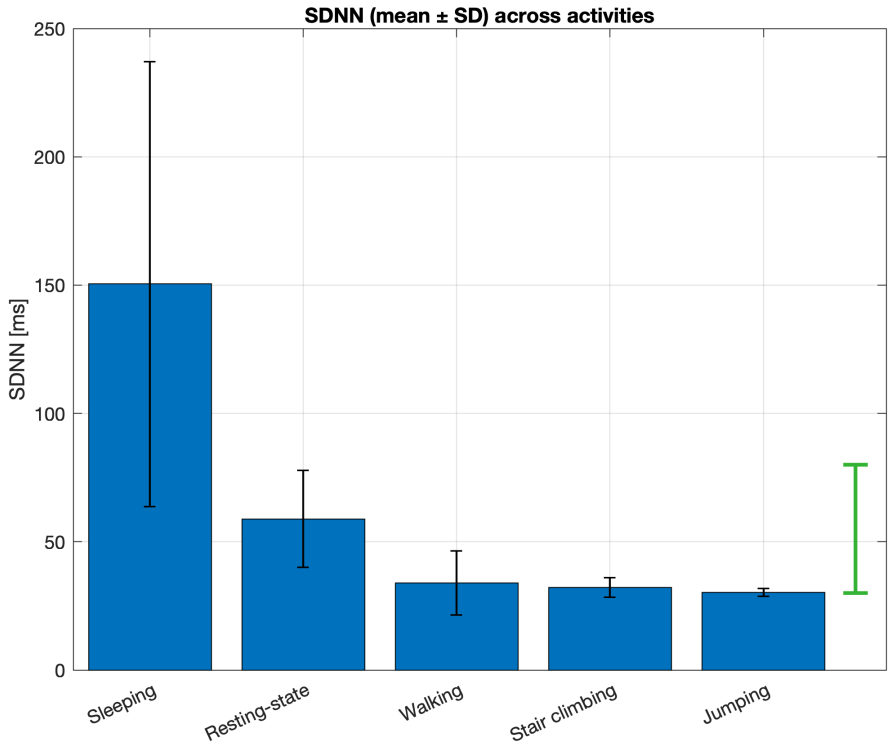

Figure 4.6: SDNN (mean ± SD) across activities. The green band indicates the physiological range at rest.

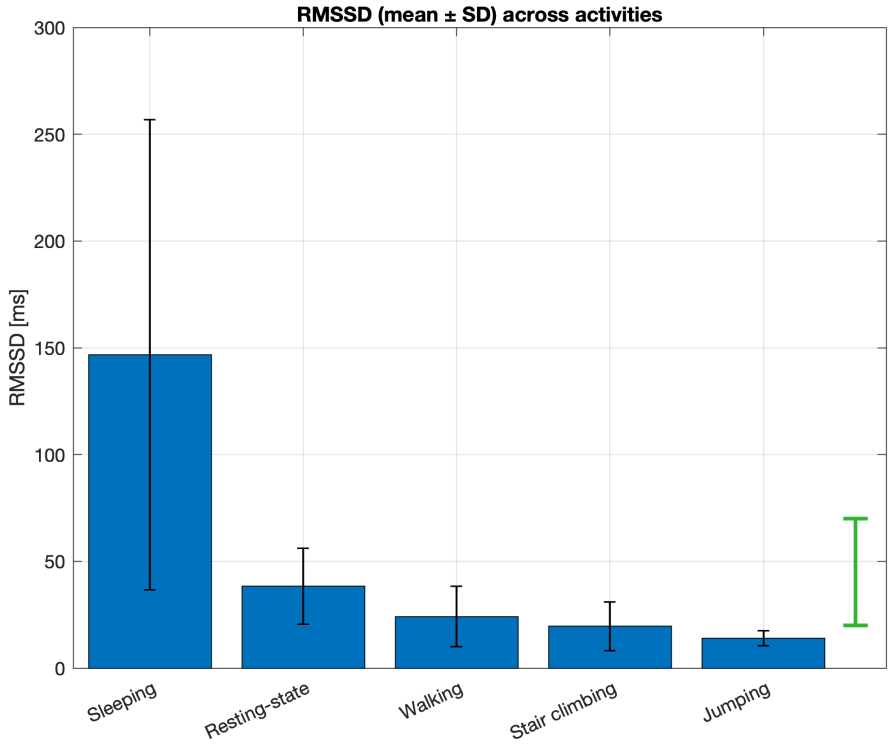

Figure 4.7: RMSSD (mean ± SD) across activities. The green band indicates the physiological range at rest.

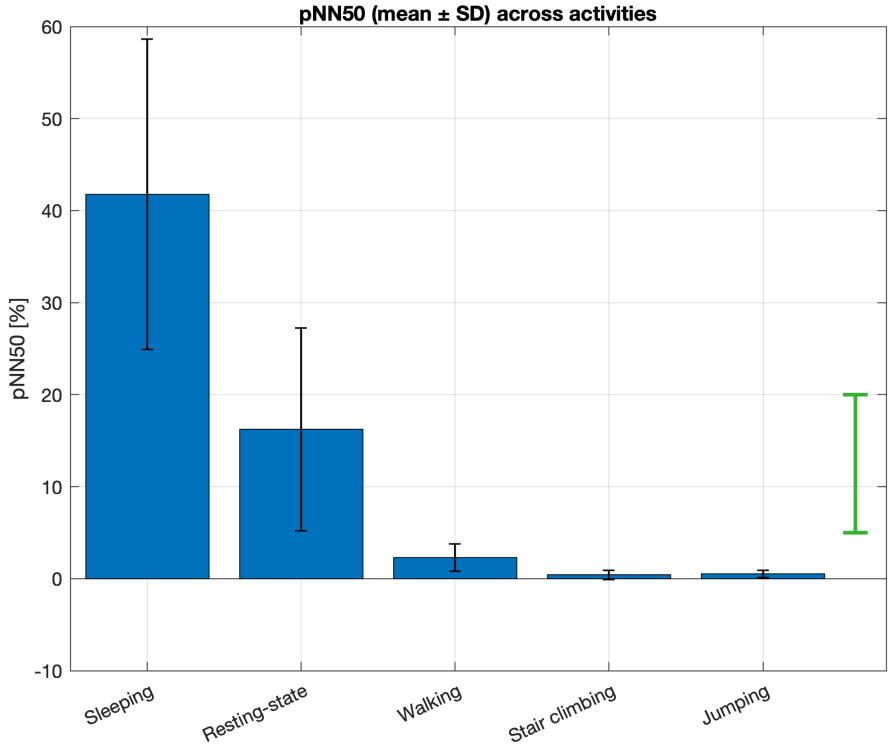

Figure 4.8: pNN50 (mean ± SD) across activities. The green band indicates the physiological range at rest.

As shown in Fig. 4.5, HR shows a progressive increase as the activity becomes more dynamic, rising from about 60 bpm during sleeping to approximately 120 bpm during stair

climbing and jumping. This trend agrees with the increased physiological demand associated with physical activities, which requires a higher cardiac output to sustain the metabolic needs of the body [11].

In contrast, short-term HRV metrics such as SDNN, RMSSD, and pNN50 exhibit an opposite behavior, progressively decreasing as the activity intensity increases (Figures 4.6-4.7). A pronounced difference in HRV metrics can be observed between sleeping and all the other conditions. In particular, SDNN and RMSSD during sleeping reach values around 150 ms, while for the other activities these metrics drop below approximately 50 ms, except for SDNN during resting-state, which remains slightly above this value. Similarly, the pNN50 value during sleeping (around 40%) dramatically decreases across the other conditions (Fig. 4.8), reaching values close to zero for stair climbing and jumping. Overall, the values of all extracted HRV metrics fall within the physiological ranges reported in the reference standards for HRV analysis [11].

From these results two main conclusions can be drawn. First, the values obtained are consistent with the expected physiological modulation of the autonomic nervous system across different activity levels. During sleep, the predominance of parasympathetic activity leads to higher short-term HRV values, whereas during challenging physical conditions the sympathetic activation becomes dominant, resulting in higher HR and a substantial reduction in beat-to-beat variability [11, 34].
Second, this behavior confirms that the estimated HR and HRV metrics are physiologically plausible, highlighting the consistency of the proposed signal processing pipeline, even under dynamic conditions.

4.2.3 RR Estimation Results

This section reports the results related to RR estimation obtained from the wearable patch. As done for HR and HRV metrics extraction, this section focuses on the first patch configuration, as the second placement provide a limited number of reliable trials also for respiratory analysis. As described in Section 3.4.3, RR was estimated directly from the bioimpedance-based signal (BioZ), and indirectly through ECG-derived respiration (EDR) signal. Similarly to HR and HRV analysis, the results are first presented at the trial level and then summarized at the activity level to highlight differences across activities. In addition, the agreement between the two estimation methods is investigated.

4.2.3.1 Trial Level Results

This subsection presents the RR estimated across dynamic trials using both the two methods. Similarly to HR and HRV section, results related to resting-state and sleeping were not reported at this level of analysis due to the large number of available trials for these conditions. Figures below show the obtained results for walking (Fig. 4.9), stair climbing (Fig. 4.10), and jumping trials (Fig. 4.11), respectively.

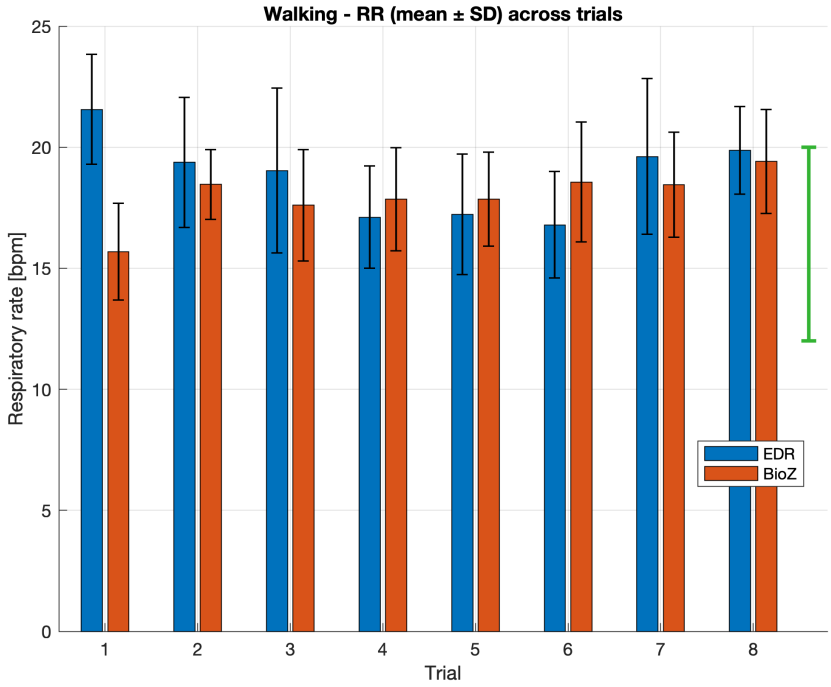

Figure 4.9: RR (mean ± SD) for each walking trial estimated from bioimpedance-based signal (BioZ) and EDR signal. The green band indicates the physiological range.

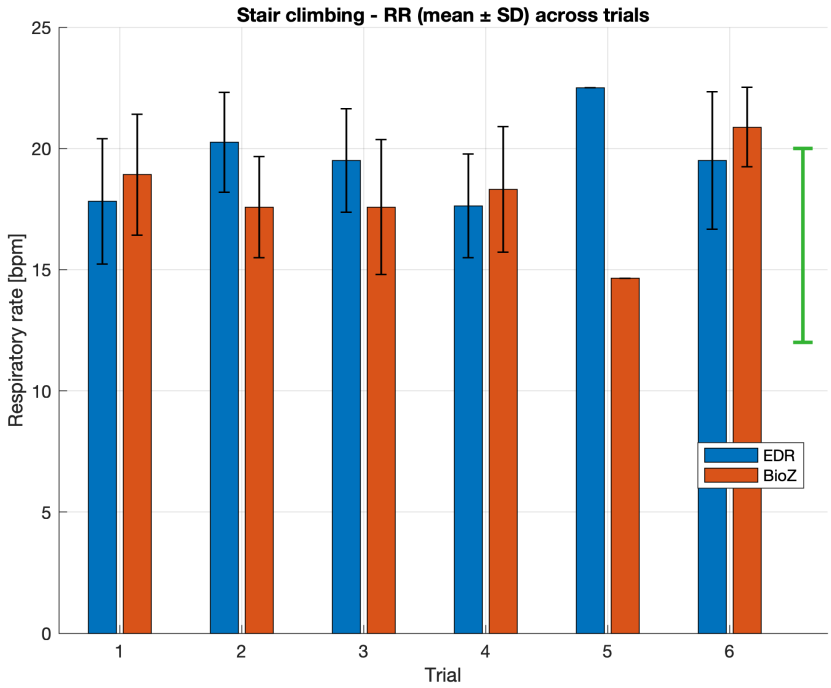

Figure 4.10: RR (mean ± SD) for each stair climbing trial estimated from bioimpedance-based signal (BioZ) and EDR signal. The green band indicates the physiological range.

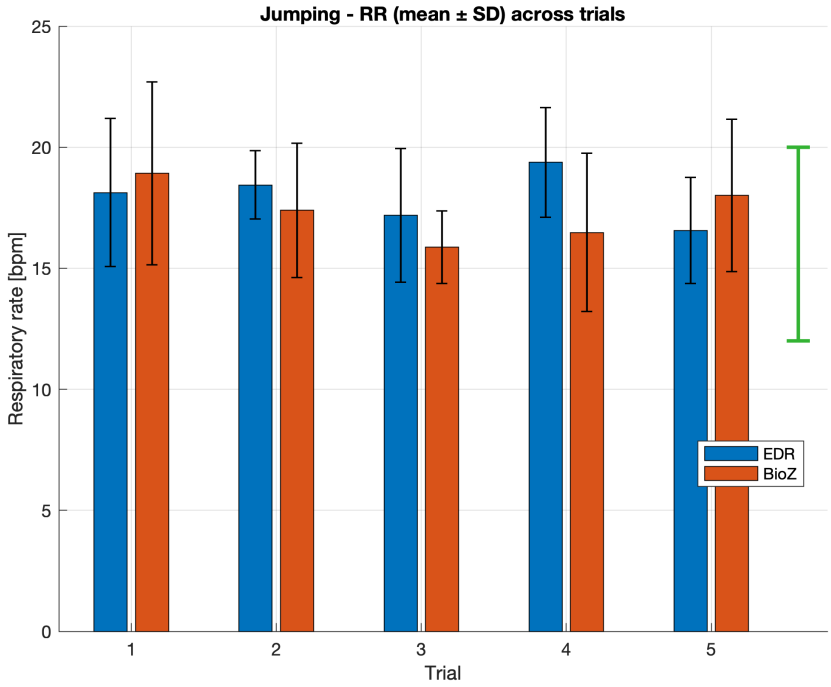

Figure 4.11: RR (mean ± SD) for each jumping trial estimated from bioimpedance-based signal (BioZ) and EDR signal. The green band indicates the physiological range.

As shown in Figures 4.9–4.11, for walking trials, RR values generally range between about 16 and 21 bpm, with moderate variability across trials and good agreement between the two estimation methods. Similar behavior is observed for stair climbing and jumping, where the two methods provide comparable estimates despite some variability between trials. However, a notable discrepancy between the two methods can be observed for stair climbing trial n.5. To further investigate this difference, Fig. 4.12 reports an illustrative example of the respiratory signals derived both from bioimpedance measurement and ECG signal for 1-min window of this trial.

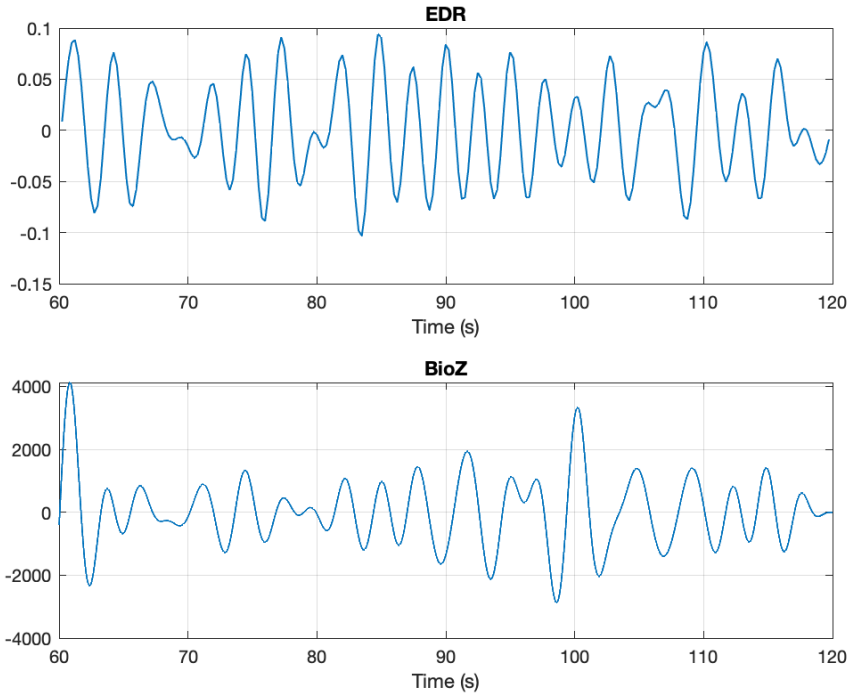

Figure 4.12: Example of respiratory signals obtained from 1-min window of stair climbing (trial n.5). ECG-derived respiration signal (upper trace) and bioimpedance-based signal (lower trace).

From Fig. 4.10, it can be observed a difference in frequency between the two respiratory sinusoids, explaining the discrepancy between RR estimates. This behavior can be led by the reduced signal quality, affecting both direct and indirect estimation, and by the limited number of windows available for this specific task (n=3).

4.2.3.2 Activity Level Results

This subsection presents the RR estimates summarized at the activity level. In this case, the RR values obtained for individual trials are aggregated to provide an overview of the average respiratory trend associated with each activity.
Fig. 4.13 illustrates the RR estimated across the different activities using both bioimpedance-based signal and EDR signal.

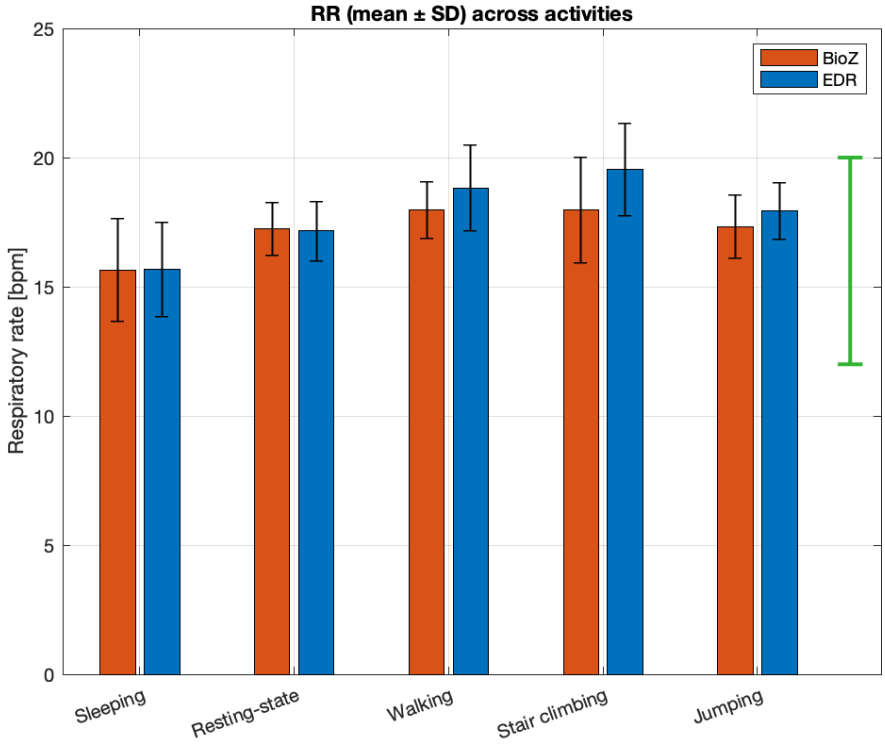

Figure 4.13: RR (mean ± SD) across activities derived from bioimpedance-based signal (BioZ) and EDR signal. The green band indicates the physiological range.

As shown in Fig. 4.13, the RR values obtained with both methods fall within the physiological ranges typically reported in the literature for resting conditions (~14–16 bpm) and moderate physical activities (~18–20 bpm) [55]. In particular, a gradual increase in RR can be observed from stationary conditions to more challenging activities. Sleeping and resting-state exhibit the lowest RR, while walking and stair climbing show higher values, reflecting the increased respiratory demand associated with physical effort.
Regarding the comparison between the two estimation approaches, the results indicate overall a good agreement between estimates using bioimpedance measurement and EDR signal across all activities. Their similar variability also suggest that both signals capture the underlying respiratory dynamics consistently.

Overall, these observations indicate that the proposed framework provides physiologically plausible RR estimates, even during dynamic and challenging activities. This result is particularly relevant for the indirect respiratory estimation derived from the ECG signal, which required multiple signal processing steps to extract the EDR signal. The robustness of the developed pipeline provided consistent respiratory estimates despite noisy conditions typical of wearable recordings.
Furthermore, the good agreement observed between estimates derived from the two methods suggests that EDR signal can be also employed for respiratory monitoring in wearable cardiorespiratory systems.

Chapter 5

Conclusion

5.1 Summary of the Work

Wearable cardiorespiratory monitoring is essential for detecting pathological patterns related to cardiovascular diseases or for providing physiological information in subjects experiencing transient events, such as stress-induced episodes. However, wearable applications are inherently affected by multiple noise sources and motion artifacts, which are typical of real-life acquisition conditions. Therefore, the use of robust signal processing strategies is essential for the reliable extraction of HR, HRV, and RR.

To address these challenges, this work first aimed to provide a solid framework for the reliable extraction of cardiorespiratory parameters from ECG and respiratory recordings under dynamic conditions. The proposed framework included ECG denoising using both traditional bandpass filtering and a singular value decomposition (SVD) approach, R-peak detection through a continuous wavelet transform (CWT)-based method, and cardiorespiratory feature extraction. Second, practical guidance for future studies is provided by assessing the impact of electrode placement on signal quality across daily activities using a developed artifact detection algorithm.

Overall, the implemented CWT-based R-peak detection method achieved good performance even during dynamic activities, consequently providing physiologically plausible HR and HRV time-domain metrics. Moreover, the RR estimates derived from the indirect ECG-derived respiration (EDR) signal showed good agreement with RR directly estimated using the bioimpedance measurement obtained from the respiratory sensor integrated in the wearable device. Regarding the comparative analysis of patch positioning, a substantial difference between the two evaluated electrode configurations (central thoracic and left side trunk locations) emerged in terms of the percentage of good-quality signal and correctly detected peaks. In particular, the mid-sternal thoracic positioning ensured greater robustness to motion artifacts, especially during dynamic activities.

These observations suggest that the developed signal processing framework for the extraction of cardiorespiratory parameters is sufficiently reliable even under noisy wearable conditions. Furthermore, the good agreement obtained between the two RR estimation methods indicates that the EDR signal can be effectively used for respiratory analysis in wearable applications.

5.2 Limitations

Despite the promising results obtained in this study, some limitations should be noted.
While the development phase, including algorithm design and preliminary testing, relied on a relatively large amount of data (approximately 22 hours of recordings collected from three different subjects), the evaluation phase conducted during daily activities was limited to a single-subject feasibility analysis. Consequently, the results obtained in this phase should be interpreted with caution and cannot be considered as a comprehensive validation of the proposed framework.
Furthermore, the number of trials involving dynamic activities was relatively limited. This was partly due to the reduced signal quality observed under motion conditions, which led to the exclusion of several trials from the analysis. As a result, although the proposed pipeline demonstrated robustness during motion-based tasks, further studies involving a larger number of subjects and a broader set of trials are required to better assess the overall applicability of the proposed approach.

5.3 Future Work

Future research should focus on extending the proposed work toward clinical applications. First, a clinical validation on pathological datasets is required to assess the performance of the pipeline in subjects affected by cardiovascular or neurological disorders.
Another important direction concerns the implementation of the developed signal processing pipeline in a real-time monitoring system, enabling continuous extraction of cardiorespiratory parameters directly on wearable devices during daily-life monitoring.
Future studies may also investigate cardiorespiratory coupling mechanisms derived from the joint analysis of cardiac and respiratory signals. In addition, the integration of accelerometer data could support motion artifact detection and provide contextual information about the subject's activity level.
Finally, event detection strategies based on the extracted physiological features could be explored to identify abnormal events in patients experiencing cardiac arrhythmias, stress-induced episodes, or seizure-like events.

Bibliography

[1] M. Brennan, M. Palaniswami, and P. Kamen, "Do existing measures of Poincaré plot geometry reflect nonlinear features of heart rate variability?," *IEEE Transactions on Biomedical Engineering*, vol. 48, pp. 1342–1347, Nov. 2001.

[2] M. Di Cesare, P. Perel, S. Taylor, C. Kabudula, H. Bixby, T. A. Gaziano, D. V. McGhie, J. Mwangi, B. Pervan, J. Narula, D. Pineiro, and F. J. Pinto, "The heart of the world," *Global Heart*, vol. 19, p. 11, Jan. 2024.

[3] P. Tripathi, A. Kumar, R. Komaragiri, and M. Kumar, "A review on computational methods for denoising and detecting ECG signals to detect cardiovascular diseases," *Archives of Computational Methods in Engineering*, vol. 29, pp. 1–40, 10 2021.

[4] C. E. King and M. Sarrafzadeh, "A survey of smartwatches in remote health monitoring," *Journal of Healthcare Informatics Research*, vol. 2, pp. 1–24, 2018.

[5] S. Hwang and S. Lee, "Wristband-type wearable health devices to measure construction workers' physical demands," *Automation in Construction*, vol. 83, pp. 330–340, 2017.

[6] M. Li, W. Xiong, and Y. Li, "Wearable measurement of ECG signals based on smart clothing," *International Journal of Telemedicine and Applications*, vol. 2020, no. 1, p. 6329360, 2020.

[7] A. Ponnusamy, J. L. Marques, and M. Reuber, "Heart rate variability measures as biomarkers in patients with psychogenic nonepileptic seizures: potential and limitations," *Epilepsy & Behavior*, vol. 22, pp. 685–691, Dec. 2011.

[8] S. J. van der Kruijs, K. E. Vonck, G. R. Langereis, L. M. Feijs, N. M. Bodde, R. H. Lazeron, E. Carrette, P. A. Boon, W. H. Backes, J. F. Jansen, A. P. Aldenkamp, and P. J. Cluitmans, "Autonomic nervous system functioning associated with psychogenic nonepileptic seizures: Analysis of heart rate variability," *Epilepsy Behavior*, vol. 54, pp. 14–19, 2016.

[9] M. Raggi and L. Mesin, "Denoising the ECG from the EMG using stationary wavelet transform and template matching," *Electronics*, vol. 14, no. 17, 2025.

[10] S. Chatterjee, R. S. Thakur, R. N. Yadav, L. Gupta, and D. K. Raghuvanshi, "Review of noise removal techniques in ECG signals," *IET Signal Processing*, vol. 14, no. 9, pp. 569–590, 2020.

[11] Task Force of the European Society of Cardiology and the North American Society of Pacing and Electrophysiology, "Heart rate variability. standards of measurement, physiological interpretation, and clinical use," *European Heart Journal*, vol. 17, pp. 354–381, Mar. 1996.

[12] J. A. Hirsch and B. Bishop, "Respiratory sinus arrhythmia in humans: how breathing pattern modulates heart rate," *American Journal of Physiology – Heart and Circulatory Physiology*, vol. 241, pp. H620–H629, Oct. 1981.

[13] L. Brown and S. Arunachalam, "Real-time estimation of the ECG-derived respiration (EDR) signal," *Biomedical sciences instrumentation*, vol. 45, pp. 59–64, 02 2009.

[14] R. E. Siciliano, A. S. Anderson, and B. E. Compas, "Autonomic nervous system correlates of posttraumatic stress symptoms in youth: Meta-analysis and qualitative review," *Clinical Psychology Review*, vol. 92, p. 102125, 2022.

[15] K. McNamara, H. Alzubaidi, and J. K. Jackson, "Cardiovascular disease as a leading cause of death: how are pharmacists getting involved?," *Integrated Pharmacy Research and Practice*, vol. 8, pp. 1–11, 2019.

[16] P. Lyakhov, M. Kiladze, and U. Lyakhova, "System for neural network determination of atrial fibrillation on ECG signals with wavelet-based preprocessing," *Applied Sciences*, vol. 11, no. 16, 2021.

[17] P. Hoyland, N. Hammache, A. Battaglia, J. Oster, J. Felblinger, C. de Chillou, and F. Odille, "A paced-ECG detector and delineator for automatic multi-parametric catheter mapping of ventricular tachycardia," *IEEE Access*, vol. 8, pp. 223952–223960, 2020.

[18] M. R. Bigler, P. Zimmermann, A. Papadis, and C. Seiler, "Accuracy of intracoronary ECG parameters for myocardial ischemia detection," *Journal of Electrocardiology*, vol. 64, pp. 50–57, 2021.

[19] E. Prabhakararao and S. Dandapat, "Myocardial infarction severity stages classification from ECG signals using attentional recurrent neural network," *IEEE Sensors Journal*, vol. 20, no. 15, pp. 8711–8720, 2020.

[20] A. I. Diadyk, N. T. Vatutin, O. M. Maiakova, V. A. Agupova, O. S. Chernykh, S. I. Malovichko, and A. E. Bagriĭ, "Rol' kholterovskogo monitorirovaniia ekg v diagnostike sinkopal'nykh sostoianiĭ [The role of Holter ECG monitoring in the diagnosis of syncopal states]," *Terapevticheskii Arkhiv*, vol. 63, no. 12, pp. 60–62, 1991. Article in Russian.

[21] S. Kaplan Berkaya, A. K. Uysal, E. Sora Gunal, S. Ergin, S. Gunal, and M. B. Gulmezoglu, "A survey on ECG analysis," *Biomedical Signal Processing and Control*, vol. 43, pp. 216–235, 2018.

[22] R. Avram, G. H. Tison, K. Aschbacher, P. Kuhar, E. Vittinghoff, M. Butzner, R. Runge, N. Wu, M. J. Pletcher, G. M. Marcus, and J. Olgin, "Real-world heart rate norms in the health eheart study," *npj Digital Medicine*, vol. 2, p. 58, June 2019.

[23] A. K. Reimers, G. Knapp, and C. D. Reimers, "Effects of exercise on the resting heart rate: A systematic review and meta-analysis of interventional studies," *Journal of Clinical Medicine*, vol. 7, p. 503, Dec. 2018.

[24] U. R. Acharya, K. P. Joseph, N. Kannathal, C. M. Lim, and J. S. Suri, "Heart rate variability: a review," *Medical & Biological Engineering & Computing*, vol. 44, pp. 1031–1051, Dec. 2006.

[25] H. K. Chen, Y. F. Hu, and S. F. Lin, "Methodological considerations in calculating heart rate variability based on wearable device heart rate samples," *Computer Methods in Biology and Medicine*, vol. 102, pp. 396–401, Nov. 2018.

[26] A. Romigi, G. Ricciardo Rizzo, F. Izzi, M. Guerrisi, M. Caccamo, F. Testa, D. Centonze, N. B. Mercuri, and N. Toschi, "Heart rate variability parameters during psychogenic non-epileptic seizures: Comparison between patients with pure pnes and comorbid epilepsy," *Frontiers in Neurology*, vol. 11, p. 713, Aug. 2020.

[27] F. Shaffer and J. P. Ginsberg, "An overview of heart rate variability metrics and norms," *Frontiers in Public Health*, vol. 5, p. 258, Sept. 2017.

[28] S. Akselrod, D. Gordon, F. A. Ubel, D. C. Shannon, A. C. Berger, and R. J. Cohen, "Power spectrum analysis of heart rate fluctuation: a quantitative probe of beat-to-beat cardiovascular control," *Science*, vol. 213, pp. 220–222, July 1981.

[29] B. Pomeranz, R. J. Macaulay, M. A. Caudill, I. Kutz, D. Adam, D. Gordon, K. M. Kilborn, A. C. Barger, D. C. Shannon, and R. J. Cohen, "Assessment of autonomic function in humans by heart rate spectral analysis," *American Journal of Physiology – Heart and Circulatory Physiology*, vol. 248, pp. H151–H153, Jan. 1985.

[30] C. P. Subbe, R. G. Davies, E. Williams, P. Rutherford, and L. Gemmell, "Effect of introducing the modified early warning score on clinical outcomes, cardiopulmonary arrests, and intensive care utilisation in acute medical admissions," *QJM: An International Journal of Medicine*, vol. 94, pp. 521–526, Oct. 2001.

[31] C. Orphanidou, S. Fleming, S. Shah, and L. Tarassenko, "Data fusion for estimating respiratory rate from a single-lead ECG," *Biomedical Signal Processing and Control*, vol. 8, no. 1, pp. 98–105, 2013.

[32] C. O'Brien and C. Heneghan, "A comparison of algorithms for estimation of a respiratory signal from the surface electrocardiogram," *Computers in Biology and Medicine*, vol. 37, no. 3, pp. 305–314, 2007.

[33] D. Cysarz, R. Zerm, H. Bettermann, M. Frühwirth, M. Moser, and M. Kröz, "Comparison of respiratory rates derived from heart rate variability, ECG amplitude, and nasal/oral airflow," *Annals of Biomedical Engineering*, vol. 36, pp. 2085–2094, Dec. 2008.

[34] W. C. Dobbs, M. V. Fedewa, H. V. MacDonald, C. J. Holmes, Z. S. Cicone, D. J. Plews, and M. R. Esco, "The accuracy of acquiring heart rate variability from portable devices: A systematic review and meta-analysis," *Sports Medicine*, vol. 49, pp. 417–435, 2019.

[35] A. Aygun, H. Ghasemzadeh, and R. Jafari, "Robust interbeat interval and heart rate variability estimation method from various morphological features using wearable sensors," *IEEE Journal of Biomedical and Health Informatics*, vol. 24, pp. 2238–2250, Aug. 2020.

[36] V. Nathan and R. Jafari, "Particle filtering and sensor fusion for robust heart rate monitoring using wearable sensors," *IEEE Journal of Biomedical and Health Informatics*, vol. 22, no. 6, pp. 1834–1846, 2018.

[37] S. Hwang, J. Seo, H. Jebelli, and S. Lee, "Feasibility analysis of heart rate monitoring of construction workers using a photoplethysmography (ppg) sensor embedded in a

wristband-type activity tracker," *Automation in Construction*, vol. 71, pp. 372–381, 2016.

[38] S. Ha, C. Kim, Y. M. Chi, A. Akinin, C. Maier, A. Ueno, and G. Cauwenberghs, "Integrated circuits and electrode interfaces for noninvasive physiological monitoring," *IEEE Transactions on Biomedical Engineering*, vol. 61, pp. 1522–1537, May 2014.

[39] V. A. Ardeti, V. R. Kolluru, G. T. Varghese, and R. K. Patjoshi, "An overview on state-of-the-art electrocardiogram signal processing methods: Traditional to ai-based approaches," *Expert Systems with Applications*, vol. 217, p. 119561, 2023.

[40] J. Pan and W. J. Tompkins, "A real-time QRS detection algorithm," *IEEE Transactions on Biomedical Engineering*, vol. 32, pp. 230–236, Mar. 1985.

[41] S. Wahabi, S. Pouryayevali, S. Hari, and D. Hatzinakos, "On evaluating ECG biometric systems: Session-dependence and body posture," *IEEE Transactions on Information Forensics and Security*, vol. 9, no. 11, pp. 2002–2013, 2014.

[42] S. Gutta and Q. Cheng, "Joint feature extraction and classifier design for ECG-based biometric recognition," *IEEE Journal of Biomedical and Health Informatics*, vol. 20, no. 2, pp. 460–468, 2016.

[43] N. M. Arzeno, Z.-D. Deng, and C.-S. Poon, "Analysis of first-derivative based QRS detection algorithms," *IEEE Transactions on Biomedical Engineering*, vol. 55, no. 2, pp. 478–484, 2008.

[44] C. Levkov, G. Michov, R. Ivanov, I. Daskalov, I. Christov, and I. Dotsinsky, "Subtraction of 50 Hz interference from the electrocardiogram," *Medical & Biological Engineering & Computing*, vol. 22, pp. 371–373, 1984.

[45] D. L. Donoho and I. M. Johnstone, "Adapting to unknown smoothness via wavelet shrinkage," *Journal of the American Statistical Association*, vol. 90, no. 432, pp. 1200–1224, 1995.

[46] M. Kania, M. Fereniec, and R. Maniewski, "Wavelet denoising for multi-lead high resolution ECG signals," *Measurement science review*, vol. 7, no. 4, pp. 30–33, 2007.

[47] P. S. Hamilton and W. J. Tompkins, "Quantitative investigation of QRS detection rules using the mit/bih arrhythmia database," *IEEE Transactions on Biomedical Engineering*, vol. BME-33, no. 12, pp. 1157–1165, 1986.

[48] T. Castroflorio, L. Mesin, G. M. Tartaglia, C. Sforza, and D. Farina, "Use of electromyographic and electrocardiographic signals to detect sleep bruxism episodes in a natural environment," *IEEE Journal of Biomedical and Health Informatics*, vol. 17, no. 6, pp. 994–1001, 2013.

[49] C. Li, C. Zheng, and C. Tai, "Detection of ECG characteristic points using wavelet transforms," *IEEE Transactions on Biomedical Engineering*, vol. 42, pp. 21–28, Jan. 1995.

[50] J. P. Martínez, R. Almeida, S. Olmos, A. P. Rocha, and P. Laguna, "A wavelet-based ECG delineator: evaluation on standard databases," *IEEE Transactions on Biomedical Engineering*, vol. 51, pp. 570–581, Apr. 2004.

[51] V. Afonso, W. Tompkins, T. Nguyen, and S. Luo, "ECG beat detection using filter banks," *IEEE Transactions on Biomedical Engineering*, vol. 46, no. 2, pp. 192–202, 1999.

[52] H. Rabbani, M. P. Mahjoob, E. Farahabadi, and A. Farahabadi, "R peak detection in electrocardiogram signal based on an optimal combination of wavelet transform, hilbert transform, and adaptive thresholding," *Journal of Medical Signals and Sensors*, vol. 1, pp. 91–98, May 2011.

[53] N. V. Thakor, J. G. Webster, and W. J. Tompkins, "Estimation of QRS complex power spectra for design of a QRS filter," *IEEE Transactions on Biomedical Engineering*, vol. 31, pp. 702–706, Nov. 1984.

[54] A. Galli, E. Peri, P. Hamelmann, and M. Mischi, "Improved mECG removal and fECG extraction by integrated periodic components analysis and singular value decomposition," pp. 1–6, 2024.

[55] C. Romano, A. Nicolò, L. Innocenti, M. Bravi, S. Miccinilli, S. Sterzi, M. Sacchetti, E. Schena, and C. Massaroni, "Respiratory rate estimation during walking and running using breathing sounds recorded with a microphone," *Biosensors*, vol. 13, p. 637, June 2023.